AMI observations of Lynds dark nebulae: further evidence for anomalous cm-wave emission

Scaife, A.M.M.; Hurley-Walker, N.; Green, D.A.; Davies, M.L.; Franzen, T.M.O.; Grainge, K.J.B.; ... ; Zwart, J.T.L.

Monthly Notices
of the
ROYAL ASTRONOMICAL SOCIETY

Mon. Not. R. Astron. Soc. **400,** 1394–1412 (2009) doi:10.1111/j.1365-2966.2009.15542.x

AMI observations of Lynds dark nebulae: further evidence for anomalous cm-wave emission⋆

AMI Consortium: Anna M. M. Scaife,† Natasha Hurley-Walker, David A. Green, Matthew L. Davies, Thomas M. O. Franzen, Keith J. B. Grainge, Michael P. Hobson, Anthony N. Lasenby, Guy G. Pooley, Carmen Rodríguez-Gonzálvez, Richard D. E. Saunders, Paul F. Scott, Timothy W. Shimwell, David J. Titterington, Elizabeth M. Waldram and Jonathan T. L. Zwart

Astrophysics Group, Cavendish Laboratory, 19 J. J. Thomson Ave., Cambridge CB3 0HE

Accepted 2009 August 12. Received 2009 August 12; in original form 2009 March 9

ABSTRACT

Observations at 14.2 to 17.9 GHz made with the Arcminute Microkelvin Imager (AMI) Small Array towards 14 Lynds dark nebulae with a resolution of ≈2 arcmin are reported. These sources are selected from the Submillimetre Common-User Bolometre Array (SCUBA) observations of Visser, Richer & Chandler as small angular diameter clouds well matched to the synthesized beam of the AMI Small Array. Comparison of the AMI observations with radio observations at lower frequencies with matched *uv*-plane coverage is made, in order to search for any anomalous excess emission which can be attributed to spinning dust. Possible emission from spinning dust is identified as a source within a 2-arcmin radius of the SCUBA position of the Lynds dark nebula, exhibiting an excess with respect to lower frequency radio emission. We find five sources which show a possible spinning dust component in their spectra. These sources have rising spectral indices in the frequency range 14.2–17.9 GHz with $\alpha_{14.2}^{17.9} = -0.7 \pm 0.7$ to -2.9 ± 0.4, where $S \propto \nu^{-\alpha}$. Of these five one has already been reported, L1111, we report one new definite detection, L675 (16σ), and three new probable detections (L944, L1103 and L1246). The relative certainty of these detections is assessed on the basis of three criteria: the extent of the emission, the coincidence of the emission with the SCUBA position and the likelihood of alternative explanations for the excess. Extended microwave emission makes the likelihood of the anomalous emission arising as a consequence of a radio counterpart to a protostar or a protoplanetary disc unlikely. We use a 2-arcmin radius in order to be consistent with the *IRAS* identifications of dark nebulae, and our third criterion is used in the case of L1103 where a high flux density at 850 μm relative to the far-infrared data suggests a more complicated emission spectrum.

Key words: radiation mechanisms: general – ISM: clouds – ISM: general – radio continuum: general.

1 INTRODUCTION

Modern theoretical models of the infrared emission from dust in the diffuse interstellar medium (ISM) require a large proportion of starlight energy to be reradiated by ultrasmall grains (≈20 per cent; Draine 2003). Comparison of the observed spectra with theory suggests that a large fraction of these small grains must be in the form of polycyclic aromatic hydrocarbons (PAHs). It is supposed that in addition to their vibrational emission, these small grains will also rotate (Erickson 1957; Ferrara & Dettmar 1994; Draine & Lazarian 1998, hereafter DL98). The emission from this rotation is found, using simple thermodynamical arguments, to be in the cm-wave regime of the electromagnetic spectrum. The details of the rotational excitation and damping have been examined in detail by DL98 and their models have been found to be in good agreement with observational results.

Although the anomalous emission was originally seen as a large-scale phenomenon (Leitch et al. 1997, see also Kogut et al. 1996)

⋆We kindly request that any reference to this paper cites 'AMI Consortium: Scaife et al. 2009'.

†Issuing author – e-mail: as595@mrao.cam.ac.uk

in cosmic microwave background (CMB) observations it has also been seen to occur in a number of different types of astronomical objects, such as H II regions, dark clouds and photodissociation regions (Casassus et al. 2006; Dickinson et al. 2007; Scaife et al. 2007; AMI Consortium: Scaife et al. 2009). It is often found to be correlated with thermal dust emission, but this is not always the case (Casassus et al. 2008). A growing number of observations have detected dust-correlated cm-wave emission which is inconsistent with free–free emission. However, these few observations are not yet sufficient to make any definite observational statement about the environmental factors which influence whether emission from spinning grains will be seen towards a certain object. We hope that the observations presented here will contribute significantly to improving this knowledge.

In this paper we have imaged 14 dark molecular clouds (MCs). Our sample is selected from the submillimetre survey of dark MCs performed using the Submillimetre Common-User Bolometre Array (SCUBA) on the James Clerk Maxwell Telescope (JCMT) by Visser, Richer & Chandler (2001). Of these 14 only three are currently known to contain protostars (L944, L1014 and L1246; Visser et al. 2001; Young et al. 2004), with the remainder thought to be examples of pre-stellar cores.

The dark MCs in this sample were taken from the Lynds dark nebula catalogue (Lynds 1962) of 1802 optically selected dark clouds from the Palomar Observatory Sky Survey (POSS) plates. The SCUBA jiggle mapping function used to observe the sample restricted the field of view to 2.3-arcmin diameter. This constraint led to a selection criterion of a maximum semiminor axis of <1.1 arcmin for each cloud, which was determined from their optical size as listed in Parker (1988).

The Lynds catalogue is divided into opacity classes from 1 to 6 of which 6 is the most opaque and includes 147 clouds. The clouds observed in the SCUBA survey are all class 6 ($A_v \geq 5$ mag; Lynds 1962) and should therefore provide the highest column density of dust when searching for anomalous emission from spinning grains.

We have observed all clouds in the sample of Visser et al. (2001) which fall in the available declination range of the Arcminute Microkelvin Imager (AMI) Small Array (SA) instrument in Cambridge. The small angular size of these clouds makes them well matched to the size of the AMI SA synthesized beam. We identify excess microwave emission from the SCUBA clouds as any source which falls within a 2-arcmin radius of the SCUBA position and which shows an excess of emission relative to lower frequency radio data. In addition, any source which satisfies these two criteria but has a falling spectrum across the AMI band will be rejected as a spinning dust candidate. This allows us to distinguish those sources which may be optically thick at lower radio frequencies, but have spectra which turn over before the AMI band.

The paper is structured as follows: Section 2 describes the telescope and the observations; Section 3 details the methods we use to compare our data to lower frequency observations; Section 4 discusses each object individually and Section 5 discusses the sample as a whole and states our conclusions.

2 OBSERVATIONS

AMI comprises two synthesis arrays, one of 10 3.7-m antennas (Small Array) and one of 8 13-m antennas (Large Array), both sited at Lord's Bridge, Cambridge (AMI Consortium: Zwart et al. 2008). The telescope observes in the band 13.5–17.9 GHz with cryostatically cooled NRAO (National Radio Astronomy Observatories) indium-phosphide front-end amplifiers. The overall system temperature is approximately 25 K. The radio frequency is mixed with a 24-GHz local oscillator, down converting to an intermediate-frequency (IF) band of 6–10.5 GHz. Amplification, equalization, path compensation and automatic gain control are then applied to the IF signal. The correlator is an analogue Fourier transform spectrometer with 16 correlations formed for each baseline at path delays spaced by 26 mm. In addition both real and imaginary correlations are formed by use of 0° and 180° hybrids. From these, eight 0.75-GHz bandwidth channels are synthesized. In practice, the two lowest frequency channels (1 and 2) are not generally used due to a low response in this frequency range and interference from geostationary satellites.

Observations of 14 dark MCs from the Lynds dark nebula catalogue were made with the AMI SA telescope during the period 2007 January–May. The AMI LA was not used in this work. Here we present data for each of these regions, which are listed in Table 1. These targets were chosen from the submillimetre survey of Visser et al. (2001) as small MCs, well matched to the AMI synthesized beam, in a declination range consistent with the capabilities of the AMI at a latitude of 52°N. Each pointing was observed at least twice for at least 8 h, with the exception of L1185 which was observed only once due to poor weather.

Data reduction was performed using the local software tool REDUCE. This applies both automatic and manual flags for interference and shadowing and hardware errors. It also applies phase and amplitude calibrations; it then Fourier transforms the correlator data to synthesize frequency channels before output to disc in *uv* FITS format suitable for imaging in AIPS.

Flux calibration was performed using short observations of 3C 286 near the beginning and end of each run. We assumed I+Q flux densities for this source in the AMI SA channels consistent with the frequency-dependent model of Baars et al. (1977), $\simeq$3.3 Jy at 16 GHz. As Baars et al. measure I and AMI SA measures I+Q, these flux densities include corrections for the polarization of the calibrator source derived by interpolating from Very Large Array (VLA) 5-, 8- and 22-GHz observations.[1] A correction is also made for the changing intervening airmass over the observation. From other measurements, we find the flux calibration is accurate to better than 5 per cent (AMI Consortium: Scaife et al. 2008; AMI Consortium: Hurley-Walker et al. 2009).

The phase was calibrated using hourly interleaved observations of calibrators selected from the Jodrell Bank VLA Survey (JVAS; Patnaik et al. 1992). After calibration, the phase is generally stable to 5° for channels 4–7, and 10° for channels 3 and 8. The full width at half-maximum (FWHM) of the primary beam of the AMI SA is $\approx$20 arcmin at 16 GHz. Channels 1 and 2 are generally discarded due to heavy satellite interference.

Reduced data were imaged using the AIPS data package. Both the MEM and CLEAN deconvolution methods were employed, as outlined in the next section. CLEAN deconvolution was performed using the task IMAGR which applies a differential primary beam correction to the individual frequency channels to produce the combined frequency image. CLEAN deconvolution maps were made from both the combined channel set and for individual channels. The full set of CLEANed AMI maps is shown in Appendix A. With the exception of Fig. 2 all of the images presented in this paper were made using CLEAN deconvolution and are not primary beam corrected. MEM deconvolution is also used on occasion in this paper, for reasons

[1] http://www.vla.nrao.edu/astro/calib/manual/polcal.html

Table 1. AMI Lynds cloud sample. Column (1) gives the source name, column (2) the right ascension, column (3) the declination, column (4) lists the rms specific intensity outside the primary beam for each map, column (5) lists the optical semimajor axis of the cloud, column (6) lists the optical semiminor axis of the cloud, column (7) lists the major axis of the synthesized beam, column (8) lists the minor axis of the synthesized beam and column (9) lists the complex associated with each dark cloud.

Name	RA[a] (J2000)	Dec.[a] (J2000)	$\sigma_{\rm rms}$ (mJy beam^{-1})	Semimajor axis[b] (arcmin)	Semiminor axis[b] (arcmin)	$\Delta\theta_{\rm max}$ (arcmin)	$\Delta\theta_{\rm min}$ (arcmin)	Associated complex
L675	19 23 52.6	11 07 39	0.17	2.2	0.6	2.6	2.4	
L709	19 13 54.1	16 26 58	0.31	1.1	1.1	2.5	2.4	
L860	20 03 18.1	36 01 45	0.21	1.1	1.1	2.5	2.1	Cloud B
L917	20 39 55.1	44 08 41	0.27	1.7	0.6	2.8	2.1	Cloud B
L944	21 17 40.8	43 18 08	0.27	1.7	1.1	2.5	2.3	Cygnus rift
L951	21 20 13.0	43 31 30	0.25	2.2	0.6	2.5	2.2	Cygnus rift
L953	21 21 25.5	43 21 04	0.55	1.1	0.6	2.5	2.4	Cygnus rift
L1014	21 24 01.7	49 59 26	0.38	1.7	0.6	2.5	2.1	Cygnus rift
L1021	21 21 39.3	50 57 20	0.40	1.1	0.6	2.4	2.1	Cygnus rift
L1103	21 42 10.2	56 43 44	0.48	2.8	1.1	2.4	2.1	
L1111	21 40 27.1	57 48 10	0.29	1.7	1.1	2.4	2.1	
L1166	22 05 26.2	59 33 38	0.56	1.1	0.6	2.6	2.2	
L1185	22 29 24.5	59 09 23	1.12	2.8	0.6	2.8	2.2	
L1246	23 25 12.9	63 39 30	0.36	2.8	1.1	2.5	2.2	Cepheus OB3 complex

[a]Positions adapted from Visser et al. (2001).
[b]Parker (1988).

described in Section 3, and is implemented through the AIPS task VTESS. The broad spectral coverage of AMI allows a representation of the spectrum between 14.2 and 17.9 GHz to be made independently of other telescopes and in what follows we use the convention: $S \propto \nu^{-\alpha}$, where S is flux density, ν is frequency and α is the spectral index.

3 MULTIFREQUENCY ANALYSIS

The synthesized beam of AMI SA has FWHM $\approx$ 2–3 arcmin. This makes comparison with low-frequency surveys difficult as the GB6 (Green Bank 6-cm) survey at 4.85 GHz (Gregory et al. 1996) and the Effelsberg telescope surveys at 2.7 GHz (Fürst et al. 1990) and 1.4 GHz (Reich, Reich & Fürst 1997) have larger beams. Moreover, flux losses are important in the context of the observations presented here as all of the sample of dark clouds lie within the Galactic plane, where the emission on different scales is complex, and will be represented differently by telescopes with different effective *uv*-coverage. To constrain the spectral behaviour of these sources we employ two *uv* matching strategies which are outlined below. Similarly the information provided on these regions at 100 μm by the *IRAS* satellite and its recently reprocessed versions (Schlegel, Finkbeiner & Davis 1998; Miville-Deschênes & Lagache 2005) are at a resolution of ≈4 arcmin, larger than that of AMI. Consequently we rely on the finer resolution results of the SCUBA observations to constrain the dust properties of the clouds.

In order to obtain spectra for these sources, direct comparison with lower frequency surveys is not possible. We must therefore perform some operation on the data in order to match the observed angular scales. In the case that $b_{\rm SD} \ll b_0$, where $b_{\rm SD}$ is the beam of the single-dish telescope and b_0 is the synthesized beam of the interferometer, the two sets of visibilities and their resulting maps can be compared directly with little loss of information, since the Fourier transform of the single-dish beam, $\tilde{b}_{\rm SD}(u, v) \approx 1$ over the (u, v) range of interest. However, this is not true in the case that $b_{\rm SD}$ approaches or is greater than b_0.

For nine of our 14 Lynds clouds lower frequency radio observations are available at 1.4 GHz from the Canadian Galactic Plane Survey (CGPS; Taylor et al. 2003). The CGPS is a combination of fully sampled interferometric data and single-dish data, which provides a total power measurement of the sky with a beam of $60 \ll b_{\rm AMI} \simeq 150$ arcsec (depending on declination). For the nine clouds covered by the CGPS we can make the approximation that $\tilde{b}_{\rm SD}(u, v) \approx 1$ over the *uv* range of interest and compare *uv*-sampled CGPS data directly to our measured visibilities from AMI. However, in the case of the remaining five clouds we are limited by the resolution of the available data and can only make a map plane comparison, after convolving the CLEAN AMI map to a common resolution. This leads to two distinct analysis paths.

The details of these data reduction methods are of importance when comparing flux densities from different instruments. This is especially the case when using interferometers. We include them here to emphasize the point that when we compare AMI observations to those at lower radio frequencies we are comparing matched angular scales, unless stated otherwise.

3.1 Image reconstruction

To simulate the visibilities we take the single-dish map and multiply by the primary beam of AMI, we then fast Fourier transform (FFT) the modulated map to obtain the data in the form of visibilities. These visibilities are sampled according to the measured visibilities in the matching AMI observation. The sets of sampled visibilities are each imaged and deconvolved separately to obtain our final simulated maps.

Case 1. CGPS data, $b_{\rm SD} \ll b_0$: we use data from the CGPS archive at 1.4 GHz for simulations. These data have a resolution of $b_{\rm SD,FWHM} = 60$ arcsec. We can examine the correlation between the two data sets in both the map plane and the *uv* plane.

Case 2. Non-CGPS data, $b_{\rm SD} \gtrsim b_0$: for example, data from the Effelsberg 100-m telescope survey at 2.7 GHz. These data have a resolution of $b_{\rm SD,FWHM} = 4.3$ arcmin. In this case we cannot directly

compare the visibilities in the *uv* plane, since the data is multiplied by the Fourier transform of the convolving beam, $b_{\rm SD}$. In the map plane, however, we can recover usable data sets for comparison when the MEM method of deconvolution is applied.

In brief, when deconvolving interferometric data using the CLEAN algorithm a recovered sky will have the form

$$I(l,m)_{\rm recovered} = [I(l,m)\,B(l,m)]\,b_0(l,m), \quad (1)$$

where $I(l, m)$ is the true sky distribution, $B(l, m)$ is the primary beam response and $b_0(l, m)$ is the CLEAN beam. In the case where we sample single-dish data our input intensity distribution is no longer the true sky but instead a model sky, which is the convolution of the true sky with the single-dish beam, $I'(l, m) = I(l, m)\,b_{\rm SD}$. Since this convolution is non-associative with the multiplication by the primary beam response, the two maps cannot be quantitatively compared.

However, if instead we choose to deconvolve using an MEM method, such as the AIPS task VTESS, the primary beam response is accounted for in the fitting. MEM lets us recover

$$\begin{aligned} I(l,m)_{\rm recovered} &= I'(l,m)\,b_0(l,m) \\ &= I(l,m)\,b_{\rm SD}\,b_0(l,m). \end{aligned} \quad (2)$$

Since convolution is associative with itself we can then convolve our own AMI data to match our sampled data. We do this by deconvolving the AMI data using VTESS to recover $I(l, m)\,b_0(l, m)$ and convolving this recovered map with the single-dish beam $b_{\rm SD}$. This will result in our comparison maps, both the sampled data and the convolved AMI data, having a CLEAN beam of $b(l,m) = \sqrt{b_0(l,m)^2 + b_{\rm SD}(l,m)^2}$. We note that this process will degrade the original AMI data, however, it results in maps which have identical resolution and contain the same angular scales.

3.2 Flux extraction

The morphology of the sources in these observations is often not well described by a Gaussian fit. We therefore estimate their flux densities by removing a tilted plane fitted to the local background and integrating the remaining flux, see for example Green (2007). We do this by drawing a polygon around each source and fitting a tilted plane to the pixels around the edge of the polygon. Where an edge of the polygon crosses a region confused by another source the background is subjective and we omit this edge from the fitting. Example polygons are shown in e.g. Fig. 2 with omitted edges shown as dashed lines. Where we believe there may be some confusion as to the aperture selected in what follows we have depicted an example aperture in the same way, see the figure captions for details. Since this method is dependent to some degree on the aperture selected around the source we perform five fits for each object changing the aperture slightly each time, and take the flux density as the average of these fits. The vertices of these apertures are listed in Appendix B. We denote the variance of these fits as $\sigma^2_{\rm fit}$ and include it in the final error on the calculated flux density as

$$\sigma = \sqrt{\sigma^2_{\rm rms} + (0.05S)^2 + \sigma^2_{\rm fit}}. \quad (3)$$

Here we represent the rms fluctuations outside the primary beam measured from the map as $\sigma_{\rm rms}$ and the flux density of the source as S. This calculation assumes a conservative 5 per cent error on the flux calibration.

We note that images made using CLEAN are often systematically different to those made using MEM through VTESS. The major, although not only, difference arises due to the positive definite nature of the model assumed in VTESS. This has the effect of raising the background level in images reconstructed by VTESS relative to those made using CLEAN. Consequently it is not recommended to use these MEM reconstructions for comparison with images restored with CLEAN. Our method of flux extraction acts to mitigate this effect through subtracting a tilted plane. However, we note that we have not used MEM images for quantitative comparison except in the case of L675 where we have compared like with like. In later sections we have sometimes included a flux density recovered using an MEM map to enhance a flux spectrum, but this is purely for illustrative purposes and will be explicitly commented upon in the text. We reiterate: case (1) employs CLEAN deconvolution, case (2) employs MEM deconvolution.

3.3 Submm data

The SCUBA data of Visser et al. (2001) and Visser, Richer & Chandler (2002) in conjunction with *IRAS* data available from the literature allow us to place constraints on the thermal dust spectrum of these objects and their dust temperature, $T_{\rm d}$.

Following Andre, Ward-Thompson & Barsony (1993) we use a modified greybody spectrum of the form

$$S_\nu = B_\nu(T_{\rm d})(1 - {\rm e}^{-\tau_\nu})\Omega_{S,\nu} \quad (4)$$

to fit these data, where $B_\nu(T_{\rm d})$ is the Planck spectrum for a temperature $T_{\rm d}$ at a frequency ν. τ_ν is the optical depth of the cloud, generally assumed to be proportional to $\nu^{1.5}$ and $\Omega_{S,\nu}$ is the extent of the source at a given frequency. The inclusion of $\Omega_{S,\nu}$ allows us to account for the different source sizes seen by *IRAS* and SCUBA.

4 IDENTIFICATION OF RADIO COUNTERPARTS

In this section we describe the radio emission seen towards the Lynds dark nebulae listed in Table 1 between 14.2 and 17.9 GHz. Sources are listed in Table 2. In what follows we identify potential excess microwave emission from the SCUBA clouds as any source which falls within a 2-arcmin radius of the SCUBA position and which shows an excess of emission relative to lower frequency radio data. In addition, any source which satisfies these two criteria but has a falling spectrum across the AMI band will be rejected as a spinning dust candidate. This allows us to distinguish those sources which may be optically thick at lower radio frequencies, but have spectra which turn over before the AMI band. All errors are quoted to 1σ.

4.1 L675

L675 shows a large radio counterpart at 16 GHz. This region lies outside the limits of the CGPS data, however, it is covered by NRAO VLA Sky Survey (NVSS) at 1.4 GHz, Effelsberg at 2.7 GHz and the GB6 survey at 4.85 GHz. These data show no counterpart to the object seen in the higher frequency AMI map, see Fig. 1.

Since there is no coverage of this region by the CGPS we use our analysis case (2) to determine the spectrum of this object. Sampling data at 2.7 and 4.85 GHz from the Effelsberg 100 m telescope[2] and the GB6 survey,[3] respectively, and correcting for the beams as described in Section 3 it is immediately noticeable that

[2] http://www.mpifr-bonn.mpg.de/old_mpifr/survey.html
[3] http://skyview.gsfc.nasa.gov/cgi-bin/query.pl

Table 2. Flux densities for compact sources found within the AMI fields which have counterparts at 1.4 GHz.

Source	RA (2000.0)	Dec. (2000.0)	$S_{1.4}$ (mJy)	S_{16} (mJy)	$\alpha_{1.4}^{16}$
L709					
A	19 14 14.8	16 36 43	270 ± 27	245 ± 13	0.07 ± 0.02
L860					
A	20 03 34.2	36 08 30	43.4 ± 5.0	5.2 ± 1.1	0.88 ± 0.30
B	20 02 44.6	36 10 30	23.2 ± 2.6	14.1 ± 2.3	0.21 ± 0.11
C	20 03 10.7	36 07 15	36.6 ± 1.2	35.6 ± 2.3	0.01 ± 0.01
D	20 03 16.8	35 59 60	25.0 ± 4.1	19.6 ± 1.5	0.10 ± 0.07
E	20 03 41.5	35 55 60	17.9 ± 2.4	17.4 ± 2.8	0.01 ± 0.03
L917					
A	20 39 31.5	44 02 11	64.9 ± 6.3	66.2 ± 11.7	-0.01 ± 0.03
B	20 39 32.8	44 09 41	2.8 ± 0.7	15.0 ± 1.6	-0.69 ± 0.21
C	20 39 43.9	44 14 11	15.6 ± 3.2	17.9 ± 2.6	-0.06 ± 0.07
L944					
A	21 18 01.4	43 16 53	11.0 ± 0.5	1.3 ± 0.3	0.89 ± 0.79
B	21 17 23.0	43 11 08	17.8 ± 0.7	5.7 ± 0.9	0.47 ± 0.12
C	21 18 34.3	43 13 22	35.1 ± 1.1	9.9 ± 0.9	0.52 ± 0.10
D	21 16 45.9	43 13 37	57.6 ± 1.8	7.7 ± 0.9	0.83 ± 0.17
E	21 16 47.1	43 23 52	25.3 ± 0.9	7.4 ± 0.9	0.50 ± 0.11
L951					
A	21 20 15.8	43 37 15	190.2 ± 7.5	23.5 ± 4.4	0.89 ± 0.79
B	21 19 48.1	43 36 45	60.7 ± 2.2	9.5 ± 2.2	0.47 ± 0.12
C	21 19 23.3	43 39 30	15.7 ± 1.1	2.8 ± 0.9	0.52 ± 0.10
D	21 20 30.6	43 19 56	4.7 ± 0.5	23.9 ± 5.2	0.83 ± 0.17
L953					
A	21 20 30.6	43 19 56	4.7 ± 0.5	20.3 ± 4.8	0.60 ± 0.15
L1014					
A	21 23 49.2	49 59 11	44.5 ± 1.1	8.5 ± 1.4	0.47 ± 0.12
B	21 24 01.7	49 56 11	67.7 ± 2.4	3.9 ± 1.4	0.52 ± 0.10
C	21 23 19.7	49 59 11	194.3 ± 6.9	25.5 ± 2.6	0.89 ± 0.79
D	21 24 39.0	50 00 26	18.4 ± 0.7	4.1 ± 1.4	0.83 ± 0.17
E	21 24 53.0	49 57 11	5.9 ± 0.5	4.8 ± 1.5	0.50 ± 0.11
F	21 23 04.1	50 02 26	194.3 ± 6.9	25.3 ± 1.5	0.50 ± 0.11
L1021					
A	21 21 45.1	50 54 07	7.6 ± 0.5	4.1 ± 1.3	0.89 ± 0.79
L1103					
A	21 43 06.5	56 40 52	140.0 ± 3.9	13.4 ± 4.4	0.97 ± 0.65
B	21 41 58.4	56 36 30	17.6 ± 5.0	4.0 ± 2.1	0.61 ± 0.46
C	21 41 36.5	56 46 54	29.5 ± 5.9	22.1 ± 4.8	0.12 ± 0.14
D	21 42 13.2	56 48 28	24.3 ± 2.1	4.3 ± 2.3	0.72 ± 0.55
E	21 41 34.7	56 53 22	21.7 ± 2.3	4.3 ± 2.4	0.67 ± 0.54
F	21 41 26.5	56 53 48	20.1 ± 3.3	15.8 ± 7.7	0.10 ± 0.20
L1111					
B	21 39 55.0	57 48 59	12.2 ± 1.3	3.0 ± 0.6	0.58 ± 0.14
L1185					
A	22 29 26.5	59 07 38	66.1 ± 1.3	2.6 ± 1.6	1.33 ± 1.11
B	22 28 12.2	59 13 37	55.1 ± 1.3	63.5 ± 5.9	-0.06 ± 0.04
L1246					
A	23 24 46.0	63 29 59	9.0 ± 0.9	5.6 ± 1.1	0.20 ± 0.08
B	23 24 21.4	63 28 14	41.5 ± 1.3	2.4 ± 0.5	1.17 ± 0.31

the morphology of this object is very different at 16 GHz to that of the lower frequencies; see Fig. 2. A correlation analysis of the maps shows that the AMI and Effelsberg data have a Pearson coefficient of only 0.25, and AMI and GB6 have a slightly higher correlation coefficient of 0.38. The correlation of GB6 and Effelsberg is 0.56. However, the correlation between the AMI map and appropriately sampled IRIS 100-μm data[3] is 0.82, demonstrating that the 16 GHz emission follows the infrared emission much more closely than the low-frequency radio data. Since the object is not detected in the lower frequency maps we take the intensities at the position of the cloud at those wavelengths and regard them as upper limits on any emission. These values are $S_{2.7} \leq 6.2$ mJy beam^{-1} for

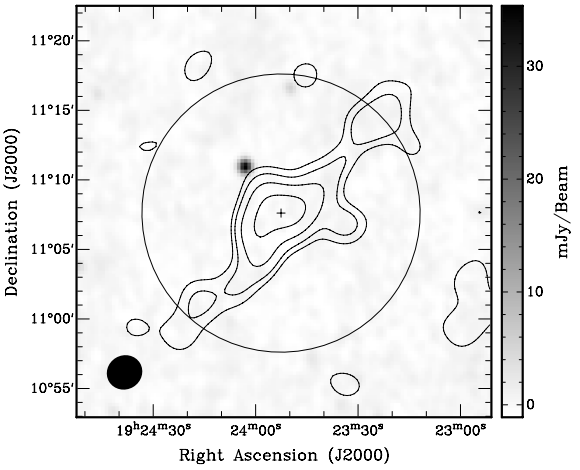

Figure 1. L675: CLEANed combined channel AMI data at 16 GHz are shown as contours. Contours are at 3, 6, 12, 18$\sigma_{\rm rms}$ etc. NVSS data are shown as grey-scale. The AMI primary beam FWHM is shown as a solid circle and the pointing centre as a cross. The AMI synthesized beam, 2.6 × 2.4 arcmin^2, is shown as a filled ellipse in the bottom left-hand corner. This map is not primary beam corrected.

Effelsberg data and $S_{4.85} \leq 3.8$ mJy beam^{-1} for the GB6 data. The spectral index, $\alpha_{2.7}^{4.85} \geq 0.84$, is consistent with a region of non-thermal emission and predicts a flux density of 1.4 mJy at 16 GHz. At the same resolution, 5.4 × 5.2 arcmin^2, the AMI emission has a flux density of $S_{16} = 20.2 \pm 1.02$ mJy. This indicates an excess of 16.4 mJy (16.1σ) at 16 GHz relative to a flat spectral index from 4.85 GHz or an excess of 18.8 mJy (18.4σ) relative to the predicted flux density from $\alpha_{2.7}^{4.85}$, assuming a source size equivalent to the beam at lower radio frequencies. Note that the noise level in the original GB6 data at this declination is ≈5 mJy beam^{-1} (Gregory et al. 1996) and in the original Effelsberg data is ≈8 mJy beam^{-1} (Fürst et al. 1990) placing all the structure within the AMI primary beam below the 2σ noise level at both frequencies.

Two further sources are evident within the primary beam of the AMI field. Of the two point sources, source 'A' lies almost exactly on the FWHM point of the beam to the north-west of L675. It appears in the six AMI channels and Effelsberg data with approximately the same flux density: $S_{2.7} = 4.3$ mJy. The best-fitting spectral index from these data is $\alpha = 0.00 \pm 0.15$. We identify this source as a region of optically thin thermal emission. Note that the derived flux density of this source at 2.7 GHz lies below the noise level of the original Effelsberg data and consequently we treat it as an upper limit. Source 'B', see Fig. 2, appears both in the NVSS map as a compact object and in the Effelsberg data as a more extended source, with flux densities of $S_{1.4} = 40.0 \pm 1.6$ mJy and $S_{2.7} = 13.1 \pm 4.9$ mJy, respectively. This indicates a steep spectrum source and, although there may be a small amount of flux at 16 GHz as indicated by the morphology of the main object, there is no identifiable discrete object at this frequency.

Although there is no object associated with L675 in the *IRAS* point source catalogue (PSC) it was part of a deep *IRAS* photometry catalogue (Clemens, Yuo & Heyer 1991; hereafter CYH91). This catalogue yielded fluxes for L675 at all four *IRAS* frequencies and a size of $\Omega_S = 39$ arcmin^2, which corresponds well to the AMI data (note that the source size from CYH91 corresponds to all flux down to the fitted background, not a Gaussian FWHM).

A greybody model, as described in Section 3.3, where $\tau_\nu \propto \nu^{1.5}$, fitted to the 100/60 μm data gives a dust temperature of $T_{\rm d} = 23.0$ K. This value agrees well with that of Clemens, Yuo & Heyer who fit a temperature of $T_{\rm d} = 23.4$ K. The model fitted to the *IRAS* data agrees with the SCUBA data at 850 μm (Visser et al. 2001) assuming the smaller angular size of 1.5 arcmin, which may be a result of the 2-arcmin chop on the SCUBA jiggle map. Using the source size of CYH91, this model predicts a flux from thermal dust emission at 16 GHz of only 0.22 μJy.

We fit three models to the AMI data points along with the upper limits at 2.7 and 4.85 GHz. The first, ignoring the lower frequency constraints, is the best-fitting power law to the AMI channel data alone. The spectral index is not well constrained: $\alpha_{\rm AMI} = -0.7 \pm 0.7$. Including the constraint given by the upper limit at 4.85 GHz requires $\alpha \leq -1.15$. The third model we fit is not a power law but the spinning dust spectrum for cold, dark MCs (DL98). Using a source dimension of $\Delta\theta = 5.5$ arcmin from the AMI map, this

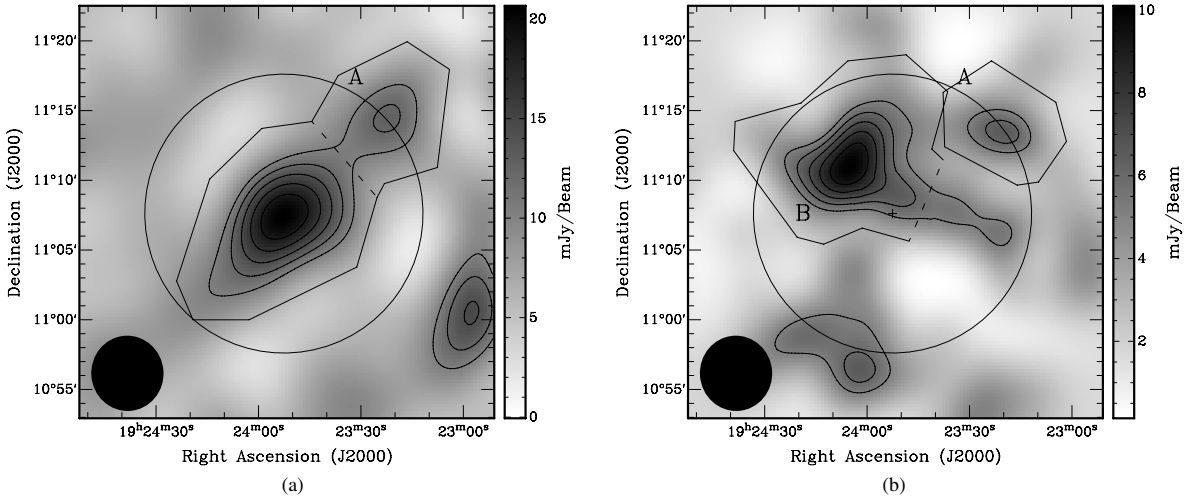

Figure 2. L675: (a) AMI 16 GHz combined channel data convolved to match the resolution of Effelsberg 2.7 GHz and (b) Effelsberg 2.7 GHz data sampled to match the *uv* coverage of AMI. Both maps have a resolution of 5.4 × 5.2 arcmin^2, shown as a filled ellipse in the bottom left-hand corner, and have been deconvolved using MEM. The AMI primary beam is shown as a circle and the pointing centre as a cross. These maps are primary beam corrected. Contours are 10 per cent from the 50 per cent level. Example flux extraction apertures are shown where a dotted line indicates an edge not used for fitting a titled plane base level, see text for details.

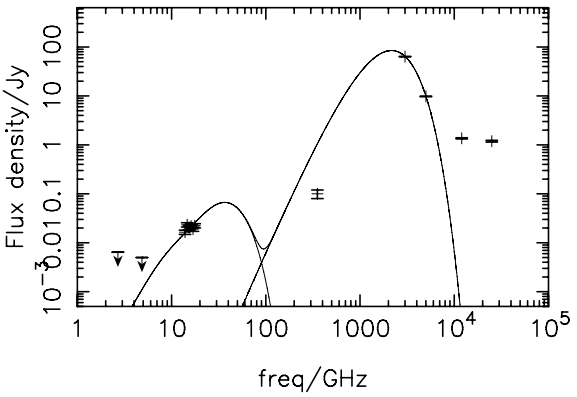

Figure 3. L675: upper limits are shown at 2.7 and 4.85 GHz from the Effelsberg 100-m telescope and the GB6 survey, respectively. These data are *uv* matched upper limits. Data at 14.2 to 17.9 GHz from AMI are shown, as are points at 850 μm (353 GHz) from Visser et al. (2001, 2002); and at 100, 60, 25 and 12 μm from CYH91. A modified greybody spectrum with $\beta = 1.5$ is fitted to the 100 and 60 μm data as described in the text and a MC spinning dust model from DL98 is fitted to the AMI data points. The combined SED is shown as a solid line.

model fits the data with $N(\mathrm{H_2}) = (2.4 \pm 1.3) \times 10^{25}\,\mathrm{m^{-2}}$ [where $N(\mathrm{H_2}) = 0.5N(\mathrm{H})$].[4] Visser et al. (2001) find a peak and averaged column density of 9 and $3.4 \times 10^{25}\,\mathrm{m^{-2}}$ for L675, consistent with this value. We note that the extent of L675 in the SCUBA map is small (≈1.5 arcmin), if this is a consequence of the SCUBA chop then the column density values may be underestimated. The full spectrum for the spinning dust model, along with the best-fitting thermal dust model, is shown in Fig. 3.

One further possibility for L675 may be that we are seeing an ultracompact H II region. A spectral index of $\alpha = -1.15$ would be broadly consistent with that expected for such a region. However, to have a turnover frequency greater than 20 GHz (assuming an electron temperature of ≈8000 K) would require an emission measure in excess of $1.2 \times 10^9\,\mathrm{pc\,cm^{-6}}$. An emission measure of this magnitude would imply a mass for the H II region of hundreds of solar masses. This is in contradiction to Visser et al. (2001) who calculate the mass of L675 to be $0.2\,\mathrm{M_\odot}$, making it the lowest mass object in our sample.

4.2 L709

There is no microwave source coincident with the pointing centre towards L709, see Fig. 4. The field is dominated by a bright radio source to the north-east of the pointing centre, denoted 'A' in Fig. 4. Source 'A' lies slightly outside the FWHM of the AMI primary beam and has a primary beam corrected continuum flux of $S_{16} = 245 \pm 13$ mJy. This is consistent with fluxes from the literature of $S_{0.365} = 374 \pm 24$ mJy (Texas), $S_{1.42} = 270 \pm 27$ mJy (Effelsberg 21 cm), $S_{2.695} = 310 \pm 31$ mJy (Effelsberg 11 cm) and $S_{4.85} = 330 \pm 29$ mJy (GB6) indicating a source with spectral index $\alpha = 0.07 \pm 0.02$; see Fig. 5. The NVSS flux density for this object is slightly lower, $S_{\mathrm{NVSS},1.4} = 218 \pm 6.6$ mJy suggesting that the source is extended. A second, and fainter, object in the field is just north-west of the pointing centre, source 'B'. This object has a flux density of $S_{16} = 6.0 \pm 0.5$ mJy in the AMI map and is most probably a combination of three unresolved point sources, which may be found in the NVSS catalogue, all falling within an AMI synthesized beam

[4] http://www.astro.princeton.edu/~draine/dust/dust.mwave.spin.html

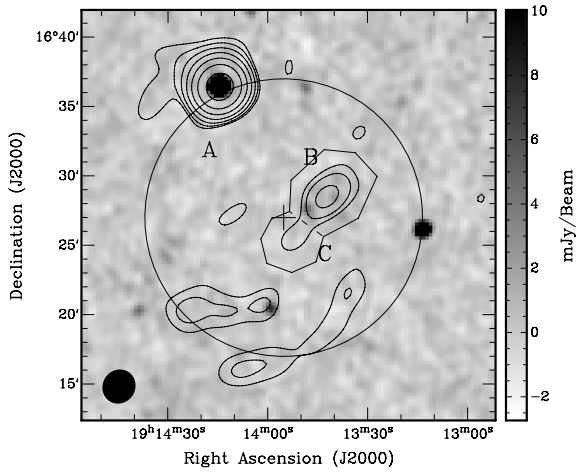

Figure 4. L709: CLEANed AMI combined channel data at 16 GHz are shown as contours with the levels as in Fig. 1. NVSS data at 1.4 GHz are shown in grey-scale and are saturated at 10 mJy peak to emphasize the structure in the map. The AMI pointing centre is indicated by a cross and the FWHM of the primary beam as a solid circle. The synthesized beam of AMI towards L709, $2.5 \times 2.4\,\mathrm{arcmin^2}$, is shown in the bottom left-hand corner as a filled ellipse. This map is not primary beam corrected. Example apertures are shown to indicate the division between sources 'B' and 'C' for flux extraction.

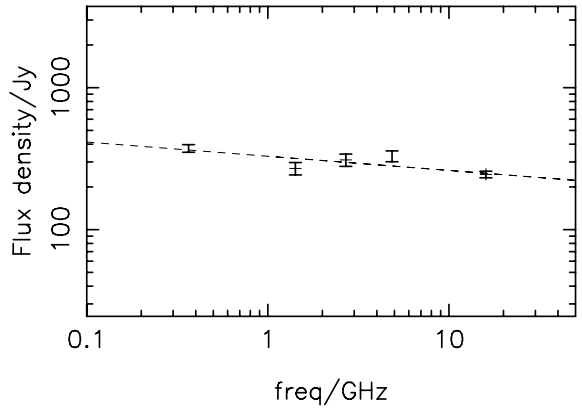

Figure 5. Radio spectrum of the L709 point source 'A'. These data points are described in the text.

at this position. These sources have a combined flux density of $S_{1.4} = 11.0 \pm 0.5$ mJy, indicating a decrease in flux at 16 GHz. The slight extension to the south of this object, 'C', is not coincident with any NVSS point sources and may be associated with L709. The object is present at the 5σ level in the combined channel map with a flux of $S_{16} = 1.61 \pm 0.31$ mJy. In the constituent channel maps the source is present with flux densities varying between 1 and 4σ. At this level of significance it is difficult to fit a reliable spectral index, however, the flux density appears to be steeply falling with increasing frequency. As the source appears point like this would suggest that source 'C' is not associated with L709 but is instead a faint steep spectrum extragalactic point source.

4.3 L860

At 16 GHz we see a ridge of emission towards L860, see Fig. 6. We investigate its spectral properties using analysis case (1). Although it possesses no obvious counterpart in the unsampled CGPS data set, a *uv* matched image shows the same structure at 1.4 GHz. To

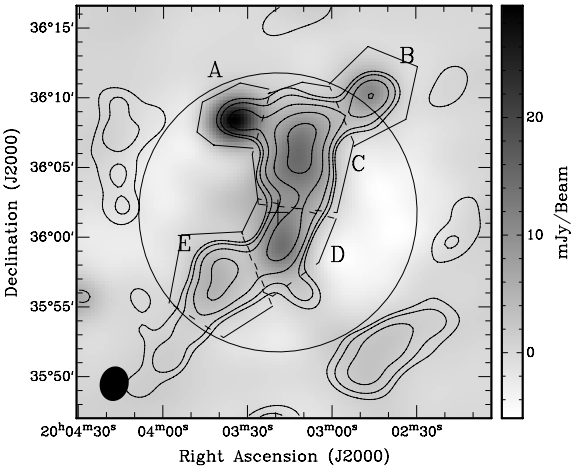

Figure 6. L860: CLEANed combined channel AMI data at 16 GHz are shown as contours with the levels as in Fig. 1. *uv* sampled CGPS data at 1.4 GHz are shown in grey-scale. The AMI pointing centre is indicated by a cross and the FWHM of the primary beam as a solid circle. The synthesized beam of AMI towards L860, 2.6×2.1 arcmin^2, is shown in the bottom left-hand corner as a filled ellipse. This map is not primary beam corrected. Example apertures for flux extraction are shown to illustrate the division between the regions denoted A–E.

the north of the field two point-like radio sources may be found (A and B), whilst the ridge of extended emission that runs north–south across the pointing centre may be divided into three distinct subregions of emission (C, D and E). The morphology of these subregions is not well described by a Gaussian model. Although both C and D might be considered to be associated with L860 the derived flux densities, see Table 2, and their spectral indices indicate that there is no excess emission present at microwave frequencies for these sources.

4.4 L917

No radio emission can be seen directly towards L917 at 16 GHz, although a ridge of emission runs north–south slightly to the west of the pointing centre, see Fig. 7. We investigate the spectral properties of this ridge primarily using analysis case (1). This ridge has three separate peaks, which are evident in both the 1.4 GHz *uv* sampled data and the AMI data at 16 GHz. We fit for the flux density of each peak separately using the flux extraction method described in Section 4.1. These peaks (A, B and C) all appear to have slightly more flux at 16 GHz than at 1.4 GHz, see Table 2. Using additional data at 2.7 GHz from the Effelsberg telescope *uv* sampled under case (2) we can fill in more of the flux spectrum. The peaks A and C show a spectrum consistent with a region of optically thin free–free emission, see Fig. 8. In 'B', the closest peak to the pointing centre we see a large excess at 16 GHz relative to 1.4 GHz, although it is not clear if this excess is caused by anomalous emission. At 2.7 GHz the emission has a largely different morphology making it difficult to constrain a spectrum using the three frequencies. A second factor which makes emission from spinning dust unlikely in this case is the spectral index across the AMI channels, $\alpha_{14.2}^{17.9} = 0.54 \pm 0.36$. With a falling spectrum this region is not a good candidate for a spinning dust emission, even considering a correction for flux loss. It can be seen from the *IRAS* data at all four frequencies that there is a ridge of dust which is spatially associated with regions A and B, see Fig. 7. However, in spite of this there is no formal *IRAS* association with L917. The change in morphology between the radio frequencies could be accounted for by this region being composed of a number of small H II regions with different turnover frequencies into the optically thin regime.

4.5 L944

The field around L944 contains a number of compact radio sources which can be seen in both the AMI data and the corresponding NVSS map, see Fig. 9. Five sources near to the pointing centre all have non-thermal spectral indices between 1.4 and 16 GHz consistent with those extrapolated from the Westerbork Northern Sky Survey (WENSS) at 327 MHz. One source is found in the AMI map just north of the pointing centre which possesses no counterpart in the NVSS data. This source is coincident with the outflow from L944 which is extended towards the north and has a flux density of $S_{16} = 3.5 \pm 0.3$ mJy in the combined channel AMI map.

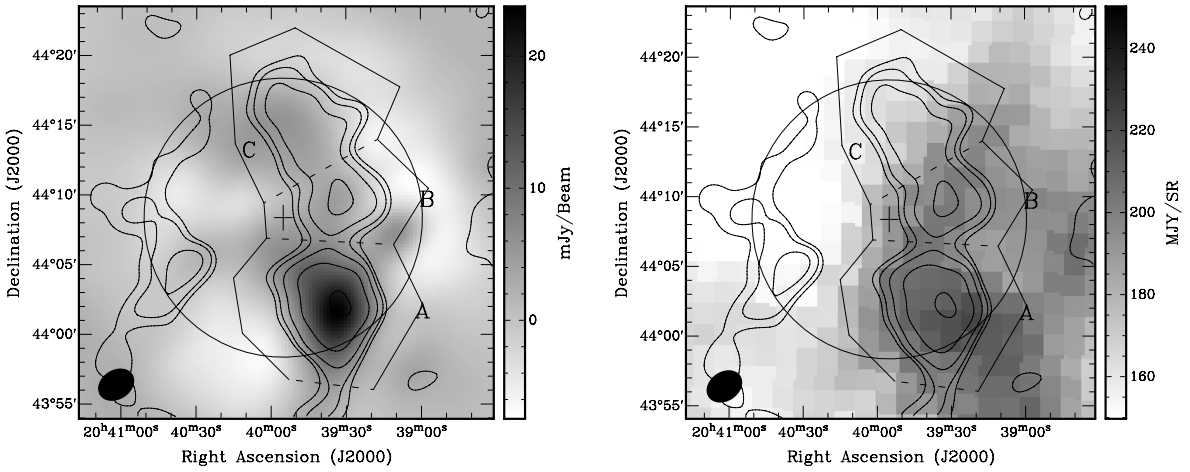

Figure 7. L917: (a) combined channel AMI data at 16 GHz are shown as contours with the levels as in Fig. 1. *uv* matched CGPS data at 1.4 GHz are shown in grey-scale. (b) AMI data at 16 GHz are shown as contours with the levels as in Fig. 1. 100-μm *IRAS* data are shown in grey-scale. The AMI pointing centre is indicated by a cross and the FWHM of the primary beam as a solid circle. These maps are not primary beam corrected. The AMI synthesized beam, 2.8×2.1 arcmin^2, is shown as a filled ellipse in the bottom left-hand corner. Example flux extraction apertures are shown to illustrate the divisions between the regions denoted A–C.

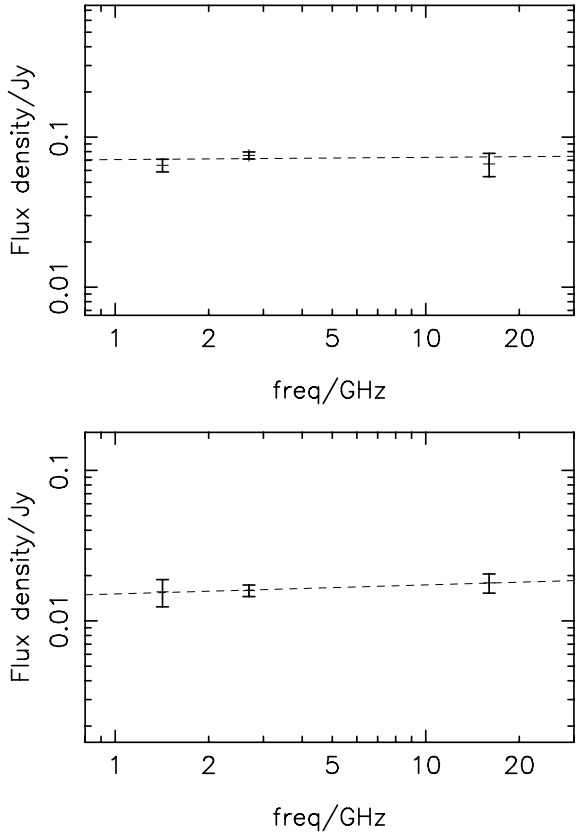

Figure 8. Above: radio spectrum of L917 region 'A'. Below: radio spectrum of L917 region 'C'. Data points are *uv* matched flux densities at 1.4, 2.7 and 16 GHz from the CGPS, Effelsberg 100-m telescope and AMI, respectively. See text for details.

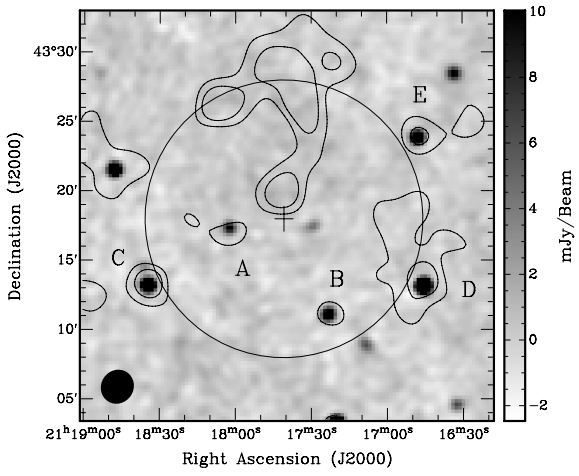

Figure 9. L944: CLEANed combined channel AMI data at 16 GHz are shown as contours with the levels as in Fig. 1. NVSS data at 1.4 GHz are shown in grey-scale and are saturated at 10-mJy peak. The AMI pointing centre is indicated by a cross and the FWHM of the primary beam as a solid circle. This map is not primary beam corrected. The synthesized beam of AMI towards L944, 2.5×2.3 arcmin^2, is shown in the bottom left-hand corner as a filled ellipse.

The spectrum of the this source appears relatively flat across the AMI band, $\alpha_{14.2}^{17.9} = -0.07 \pm 1.04$, and may be a thermal source which remains optically thick to high frequencies turning over below 16 GHz. It has no counterpart in either the NVSS data at 1.4 GHz, *uv* sampled Effelsberg data at 2.7 GHz or the GB6 data at 4.85 GHz. It is not possible to constrain the spectral index of the possible optically thick component, as the source flux at 16 GHz already lies below the noise level for both the Effelsberg data and the GB6 survey.

The short frequency lever arm of the AMI data alone makes an estimate of the spectral index from 14.2 to 17.9 GHz imprecise. However, including the constraint provided by the lack of any flux at 1.4 GHz in the NVSS data constrains the spectral index to be $\alpha_{1.4}^{17.9} \leq -1.2$. Such a spectral index could be consistent with the optically thick regime of an ultracompact/hypercompact H II region, the spectral indices of which are normally slightly shallower than $\alpha = -2$ (Franco et al. 2000).

Two obvious possibilities to explain these observations might also be cm-wave emission from a protostar within L944, or alternatively emission from a protoplanetary disc which may also extend into the cm regime. The second of these seems unlikely: protoplanetary discs are associated with later T-Tauri stars and are also extremely small in angular diameter. For the flux density measured at 16 GHz to be accounted for by the tail of the dust spectral energy distribution (SED) we would require $\beta = 0.1$, consistent with the SED of a protoplanetary disc. However, we find that the flux densities from SCUBA and *IRAS* are best fitted by $\beta = 0.8$ in agreement with Froebrich (2005). Assuming a source point like to the *IRAS* beam, this would predict a flux density from thermal dust of only 0.55 mJy at 16 GHz.

The possibility of cm-wave emission from a protostar is not unlikely. L944 is known to be a class 0 source, having extended and centrally peaked submillimetre continuum emission, which indicates an spheroidal envelope; a high ratio of submillimetre to bolometric luminosity (Froebrich 2005) and bipolar molecular outflows (Visser et al. 2002). Given these conditions it should also have an internal heating source, which would give rise to compact cm-wave emission. Previous observations of candidate protostars in the cm regime (e.g. Andre et al. 1993; Stamatellos et al. 2007) found fluxes which would not be inconsistent with that measured by AMI towards this source, however, we note that the observed AMI flux densities would be higher than the average flux density.

4.6 L951 and L953

There is no radio emission evident towards either L951 or L953, see Figs 10 and 11. The two fields overlap by a small amount – source 'D' in the L951 field is also source 'A' in the L953 field. The flux of this source agrees well between the observations and although it appears to have a rising spectrum from 1.4 to 16 GHz it has turned over by 4.85 GHz and may be found in the GB6 catalogue with a flux of $S_{4.85} = 36 \pm 5$ mJy, giving a spectral index of $\alpha_{4.85}^{16} = 0.41 \pm 0.14$. The ridge of extended emission which runs roughly north–south along the eastern edge of the L951 field and the western edge of the L953 field may be associated with an enhancement of the local infrared emission and may be seen in *IRAS* data towards the same region, see Fig. 10(b).

4.7 L1014

The L1014 field contains a number of compact sources none of which is completely coincident with the SCUBA position of the dark cloud, see Fig. 12. The two closest sources 'A' and 'B' both have falling spectral indices and are therefore not candidates for anomalous emission. Like L944, L1014 is a class 0 source (Young et al. 2004; Bourke et al. 2005). Radio cm-wave observations with the VLA have identified a candidate for the protostar at

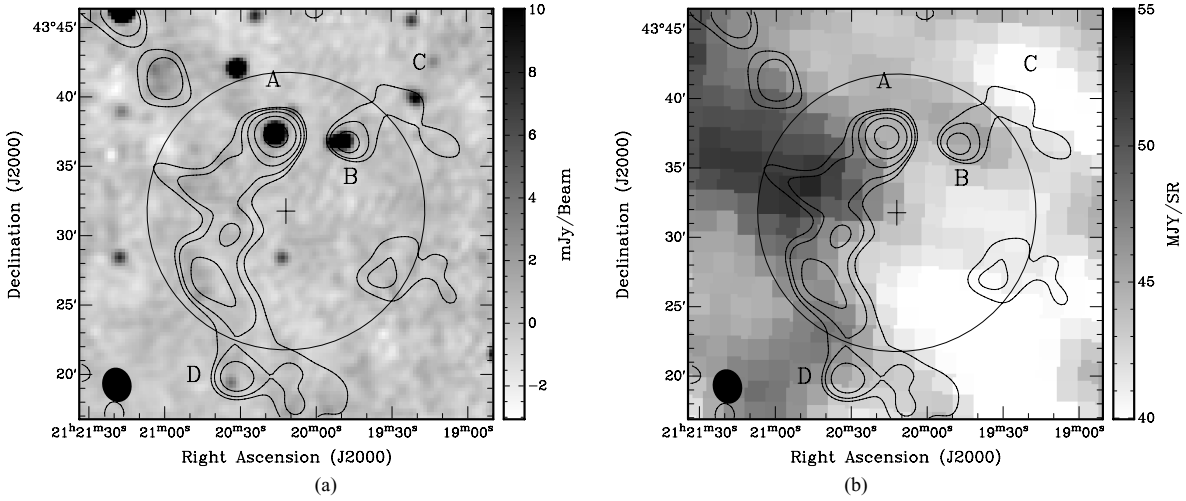

Figure 10. L951: (a) CLEANed combined channel AMI data at 16 GHz are shown as contours with the levels as in Fig. 1. CLEANed *uv* matched CGPS data at 1.4 GHz are shown in grey-scale. (b) AMI data at 16 GHz are shown as contours with the levels as in Fig. 1. 100-μm *IRAS* data are shown in grey-scale. The AMI pointing centre is indicated by a cross and the FWHM of the primary beam as a solid circle. The AMI synthesized beam, 2.5 × 2.2 arcmin^2, is shown as a filled ellipse in the bottom left-hand corner.

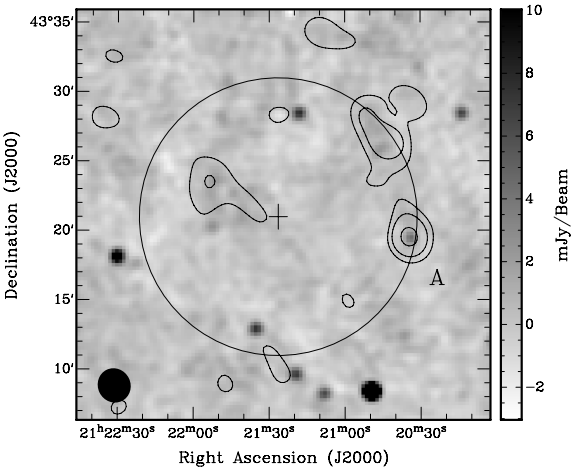

Figure 11. L953: CLEANed combined channel AMI data at 16 GHz are shown as contours with the levels as in Fig. 1. NVSS data at 1.4 GHz are shown in grey-scale and are saturated at 10-mJy peak. The AMI pointing centre is indicated by a cross and the FWHM of the primary beam as a solid circle. The AMI synthesized beam, 2.5 × 2.3 arcmin^2, is shown as a filled ellipse in the bottom left-hand corner.

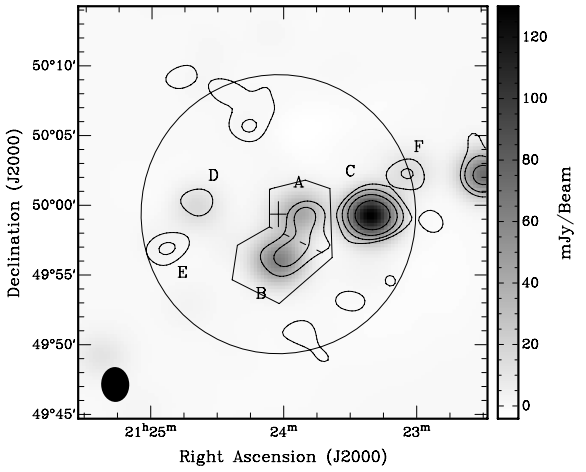

Figure 12. L1014: CLEANed combined channel AMI data at 16 GHz are shown as contours with the levels as in Fig. 1. CLEANed *uv* matched data from the CGPS at 1.4 GHz are shown in grey-scale. The AMI pointing centre is indicated by a cross and the FWHM of the primary beam as a solid circle. The AMI synthesized beam, 2.5 × 2.1 arcmin^2, is shown as a filled ellipse in the bottom left-hand corner. Example flux extraction apertures are shown to illustrate the division between sources 'A' and 'B'.

RA21^{h}24^{m}07^s.53, $\delta = +49^\circ59'08''.9$ (J2000.0) (Shirley et al. 2007). Their measurements would imply a flux density of $S_{16} = 145$ μJy at 16 GHz, well below the thermal noise in this observation.

4.8 L1021

This relatively empty field contains only one radio source which can also be identified in the lower frequency data, see Fig. 13. Its falling spectral index suggests that it is a non-thermal extragalactic point source.

4.9 L1103

This field contains a number of small diameter sources, the brightest of which, 'A', we identify as J214307+564033. Sampling the corresponding CGPS data towards L1103 reveals low-frequency counterparts to many of these, see Fig. 14. However, the object found closest to the pointing centre of this field has no lower frequency counterpart. The maximum flux towards the pointing centre from the *uv* sampled CGPS data at 1.4 GHz is 1 mJy beam^{-1}, compared to a peak flux density of 4 mJy beam^{-1} at 16 GHz. Moreover, an extended structure is obvious in the AMI data running south from the pointing centre which is not evident at 1.4 GHz. The total integrated flux of this object from the combined AMI channels is 40.1 ± 3.1 mJy. The ridge is present at all AMI frequencies and has a rising spectral index of $\alpha = -1.6 \pm 0.3$. However, the ridge has dimensions of approximately 10 × 3 arcmin^2, and at such sizes we would expect a significant amount of flux loss across the AMI band. This flux loss would have the effect of steepening a falling spectrum, or flattening a rising spectrum. Since the morphology in the 1.4-GHz data is very different we cannot use this as a model to calculate absolute flux loss. Instead we model the ridge

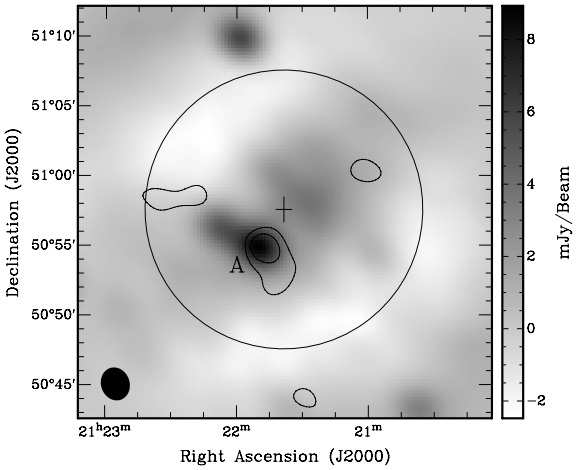

Figure 13. L1021: CLEANed combined channel AMI data at 16 GHz are shown as contours with the levels as in Fig. 1. CLEANed *uv* matched data from the CGPS at 1.4 GHz are shown in grey-scale. The AMI pointing centre is indicated by a cross and the FWHM of the primary beam as a solid circle. The AMI synthesized beam, 2.4 × 2.1 arcmin^2, is shown as a filled ellipse in the bottom left-hand corner.

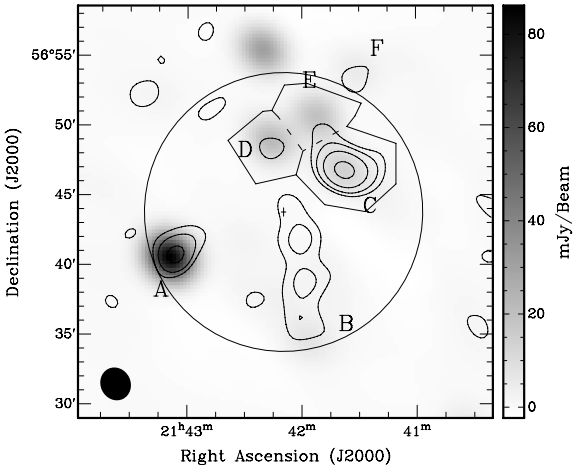

Figure 14. L1103: CLEANed combined channel AMI data at 16 GHz are shown as contours with the levels as in Fig. 1. CLEANed *uv* matched data from the CGPS at 1.4 GHz are shown in grey-scale. The AMI pointing centre is indicated by a cross and the FWHM of the primary beam as a solid circle. The AMI synthesized beam, 2.4 × 2.1 arcmin^2, is shown as a filled ellipse in the bottom left-hand corner. Example flux extraction apertures are shown to illustrate the division between those sources labelled C–E.

as a multivariate Gaussian and calculate a flux loss correction for channels 4–8, relative to channel 3. This will give us the true slope across the AMI band, if not the total power normalization. With these corrections we find a corrected spectral index of $\alpha = -2.2 \pm 0.2$. A further correction we might make is to remove the flux of the point-like object 'B' from the flux density of the ridge as a whole. However, it is unclear from a comparison of the AMI and *uv* sampled CGPS data how large the contribution of B to the ridge flux density may be. Although the ridge certainly extends to meet B, there is no clear peak at the position of the 1.4-GHz source. Consequently, since the difference in flux density across the AMI band will be small compared to the necessary increase in the error budget we chose not to subtract the flux of this object from that of the ridge as a whole. Instead we consider object 'B' as part of the ridge and simply find the integrated flux density of the entire ridge. At 1.4 and 2.7 GHz there is no apparent elongation towards the pointing centre and so the flux density is heavily dominated by the southern end of the ridge. Using *uv* matched data at 1.4 and 2.7 GHz we find a poorly constrained spectral index of $\alpha_{1.4}^{2.7} = 0.37 \pm 0.30$. Again we urge caution when considering the 2.7-GHz flux density as it is only marginally above the noise level of the original Effelsberg data.

Although, like L675, L1103 has no formal *IRAS* association it was also observed using deeper *IRAS* photometry by CYH91 and we use their measurements to constrain the far-infrared (FIR) SED. They found the size of L1103 to be $\Omega_S = 77$ arcmin^2, more consistent with the area seen by AMI than with SCUBA. Again as in the case of L675, this is perhaps not surprising given the SCUBA 120-arcsec chop. Note that the greybody spectrum which best fits the *IRAS* data points at 60 and 100 μm significantly underestimates the SCUBA flux at 850 μm when the differing angular size of the observed source is taken into account. We find a best-fitting SED with $\beta = 0.9$ and $T_{\rm d} = 37.2$ K, in good agreement with that of CYH91 who found $T_{\rm d} = 37.6$ K with β fixed at 1.

The large extension of the AMI object makes emission from either a protoplanetary disc or a single protostar unlikely, although the high dust temperature suggests that this is not a pre-stellar core as has been previously supposed. A spinning dust model with the dimension of the object fixed at $\Omega_S = 30$ arcmin^2, as suggested by the AMI data would imply an $N({\rm H}) = (4.6 \pm 0.8) \times 10^{26}$ m^{-2}. This spectrum is shown in Fig. 15.

Visser et al. (2001) comment that the distribution of material in L1103 looks as though it may have been swept up by a wind. The emission from objects with stellar winds and stars experiencing mass loss has been modelled in the past (Calabretta 1991; Casassus et al. 2007) by treating the optical depth as a power-law function of radius. These models, parametrized correctly, can lead to a rising flux density spectrum even into the mm-wave regime. We obtain a spectral index of $\alpha_{16\,{\rm GHz}}^{850\,\mu{\rm m}} = -1.14 \pm 0.13$, although we note that there has been no correction for flux losses in the flux density measurements used to calculate this index. Indeed, with no basis for a model for this source it is not possible to adequately constrain this index in order to make any quantitative comments. We note, however, that a radial power-law model is a vast oversimplification in this case as the emission is far from spherically symmetric, and also that models of this type which fit both the AMI and SCUBA data points greatly overestimate the flux densities measured at 12 and 25 μm. In addition, these winds are generally associated with more evolved protostars. L1103 is supposedly starless, having no observed outflows or *IRAS* PSC associations. However, the 12 and 25 μm flux densities of CYH91 would indicate a hotter dust component to this cloud which might suggest a class 0 object.

4.10 L1111

The subject of a separate publication, L1111 possesses a significant excess of emission relative to that found at 1.4 GHz in CGPS data *uv* sampled to match the AMI coverage (AMI Consortium: Scaife et al. 2009; see Fig. 16). Using our *uv* sampling case (2) we also confirm that there is an excess relative to the 2.7-GHz flux density. This map has significantly larger resolution (5.1 × 4.9 arcmin^2) and so the point source to the west of L1111, denoted 'B' in Scaife et al., cannot be clearly resolved from the main object. The integrated flux density of the two objects at 2.7 GHz is 15.6 ± 1.0 mJy. The spectrum of source 'B' was measured to be $\alpha = 0.43 \pm 0.18$, which would give it a flux of $S_{2.7} = 7.6^{+1.5}_{-1.3}$ mJy, leaving the object

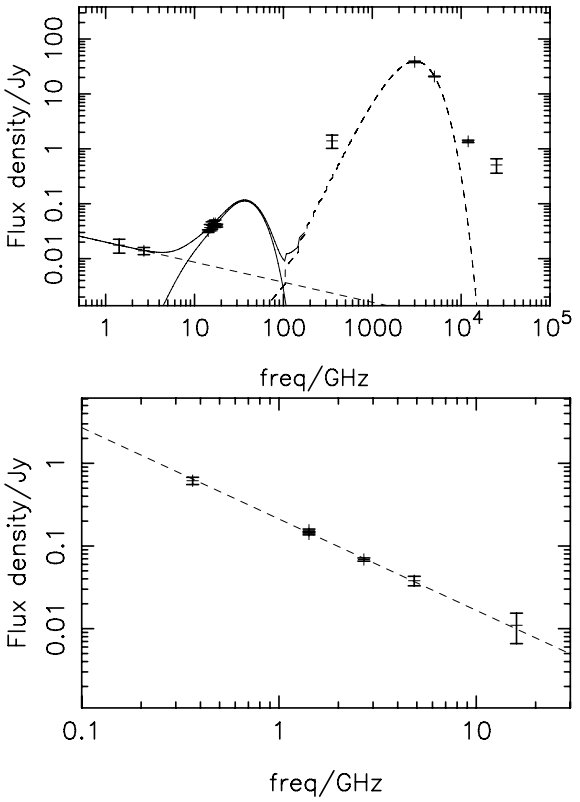

Figure 15. Top: SED of L1103. Data points are shown at 1.4 and 2.7 GHz from the CGPS and Effelsberg 100 m. These data are *uv* matched to the data at 13.8 to 17.6 GHz from AMI which are also shown. As are points at 850 μm (353 GHz) from Visser et al. (2001, 2003); and at 100, 60, 25 and 12 μm from CYH91. A modified greybody spectrum with $\beta = 1.5$ is fitted to the 850, 100 and 60 μm data as described in the text and a MC spinning dust model from DL98 is fitted to the AMI data points, see text for details. The combined SED is shown as a solid line. Bottom: SED of J214307+564033. Data points are shown at 327 MHz (WENSS; Rengelink et al. 1997), 1.4 GHz (NVSS; Condon et al. 1998; *uv* matched CGPS, this work), 2.7 GHz (*uv* matched Effelsberg 100 m, this work), 4.85 GHz (GB6; Gregory et al. 1996) and 16 GHz (AMI, this work). A best-fitting spectral index of $\alpha = 1.1 \pm 0.26$ is shown as a dashed line.

associated with L1111 a flux density of $S_{2.7} = 8.0^{+1.3}_{-1.2}$ mJy. However, the noise on the original Effelsberg data is very similar to this at 8 mJy beam^{-1}, so the *uv* sampled flux density should be viewed with caution.

Although there is no *IRAS* association with L1111, we fit a greybody spectrum to the 100-μm flux from the *IRAS* RSC Reject Catalogue (see Fig. 17). Using the 100 and 850 μm flux densities we find a best-fitting temperature of $T_{\rm d} = 20$ K using $\Omega_S = 6$ arcmin^2 measured from the SCUBA map. The spectral index across the flux loss corrected AMI data is $\alpha^{17.2}_{14.6} = -2.9 \pm 0.4$, see Scaife et al. (2009) for further details.

4.11 L1166

This object is coincident with a patch of diffuse emission seen at 1.4 GHz which has become significantly fainter at 16 GHz, see Fig. 18.

4.12 L1185

The L1185 field is relatively empty, see Fig. 19. The compact source present to the south of the pointing centre in the *uv* sampled CGPS data has a flux density of $S_{1.4} = 66.1 \pm 1.3$ mJy at 1.4 GHz and

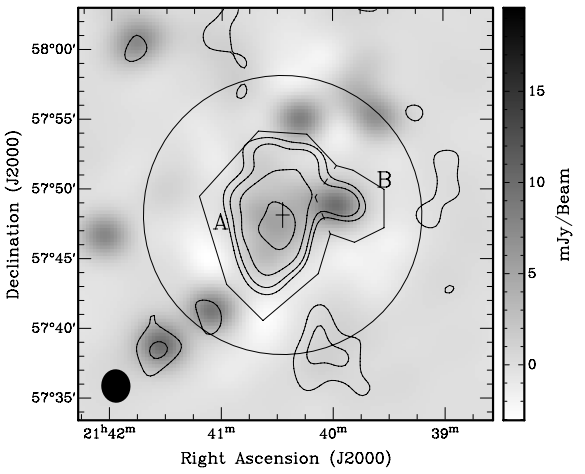

Figure 16. L1111: CLEANed combined channel AMI data at 16 GHz are shown as contours with the levels as in Fig. 1. CLEANed *uv* matched data from the CGPS at 1.4 GHz are shown in grey-scale. The AMI pointing centre is indicated by a cross and the FWHM of the primary beam as a solid circle. The AMI synthesized beam, 2.4 × 2.1 arcmin^2, is shown as a filled ellipse in the bottom left-hand corner. Example flux extraction apertures are shown to illustrate the division between the sources labelled 'A' and 'B'.

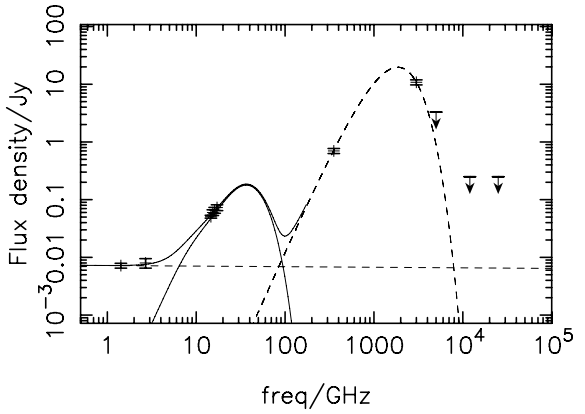

Figure 17. SED of L1111. *uv* sampled data points are shown at 1.4 and 2.7 GHz from the CGPS and Effelsberg 100 m. Data at 13.8 to 17.6 GHz from AMI are also shown. As are points at 850 μm (353 GHz) from Visser et al. (2001, 2003); and at 100, 60, 25 and 12 μm from the *IRAS* point source rejects catalogue. A power law is fitted to the data at 1.4 and 2.7 GHz which is shown as a dashed line. A modified greybody spectrum with $\beta = 1.5$ is fitted to the 850 and 100 μm data as described in the text and a MC spinning dust model from DL98 is fitted to the AMI data points, see text for details. The combined SED across the AMI band is shown as a solid line.

$S_{16} = 2.6 \pm 1.6$ mJy (2σ) in the AMI data. This gives it a poorly constrained spectral index of $\alpha^{16}_{1.4} = 1.3 \pm 1.1$, but is consistent with that derived from data at 365 MHz (Texas Survey) and the CGPS at 1.4 GHz of $\alpha^{1.4}_{0.365} = 1.6 \pm 0.6$, see Fig. 20. We therefore suggest that this is a steep spectrum extragalactic source.

4.13 L1246

L1246 is a reasonably well-studied dark cloud. It is known to contain a protostar (SMM1; Launhardt, Ward-Thompson & Henning 1997; Visser, Richer & Chandler 2001), IRAS 23228+6320, at $23^{\rm h}25^{\rm m}05\overset{\rm s}{.}6$, $+63^\circ36'34\overset{''}{.}1$ (J2000.0). The position of the *IRAS* association seems to be dominated by the 25 and 60 μm emission, with the 12 and 100 μm maps showing emission further to the east.

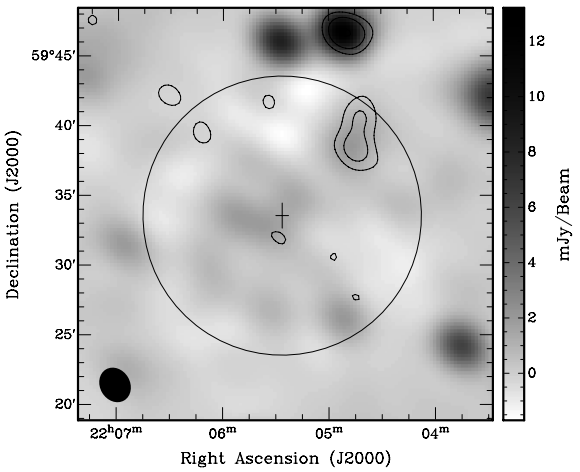

Figure 18. L1166: CLEANed combined channel AMI data at 16 GHz are shown as contours with the levels as in Fig. 1. CLEANed *uv* matched data from the CGPS at 1.4 GHz are shown in grey-scale. The AMI pointing centre is indicated by a cross and the FWHM of the primary beam as a solid circle. The AMI synthesized beam, 2.6 × 2.2 arcmin^2, is shown as a filled ellipse in the bottom left-hand corner.

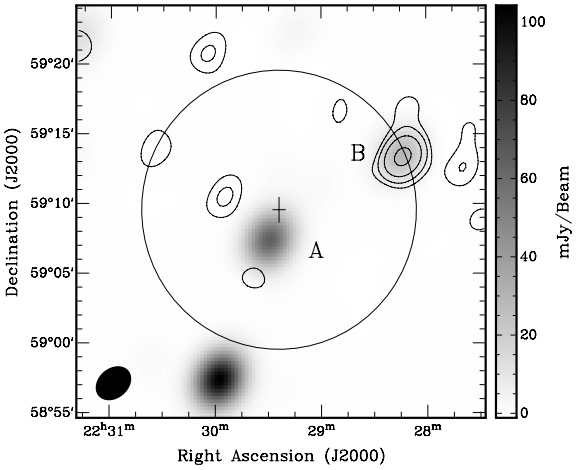

Figure 19. L1185: CLEANed combined channel AMI data at 16 GHz are shown as contours with the levels as in Fig. 1. CLEANed *uv* matched data from the CGPS at 1.4 GHz are shown in grey-scale. The AMI pointing centre is indicated by a cross and the FWHM of the primary beam as a solid circle. The AMI synthesized beam, 2.8 × 2.2 arcmin^2, is shown as a filled ellipse in the bottom left-hand corner.

The AMI map at 16 GHz shows a band of emission which traces that found at 12 μm, see Fig. 21. The northern most lobe of which is also coincident with an 8-μm point source seen in the MSX[5] image of the same region, see Fig. 21. This emission has no counterpart in the lower frequency *uv* sampled CGPS data at 1.4 GHz. The known protostar L1246 SMM1 can also be seen in the 8-μm data just to the west of the pointing centre. Two of the four PAH mid-infrared (MIR) features at 7.7 and 8.6 μm lie within MSX band A. The unidentified MSX point source coincident with the AMI emission in the L1246 field is only present within this band.

We note that although Visser et al. (2001) take the size of this cloud to be small, using the dimensions of Parker (1991) of 2.8 × 1.1 arcmin^2, the cloud appears larger in the Digital Sky Survey (DSS) plates with dimensions much closer to those measured

[5] http://irsa.ipac.caltech.edu/applications/MSX/MSX/

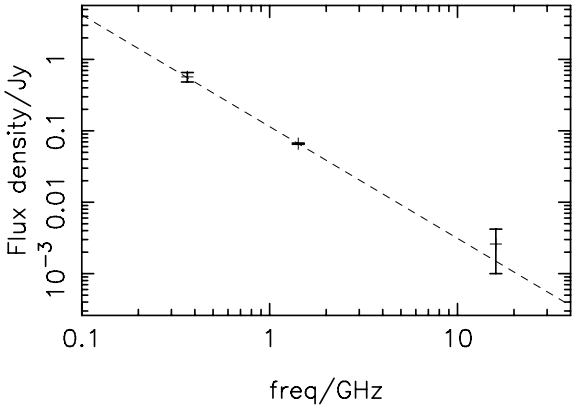

Figure 20. L1185: radio spectrum of source 'A'. Data points are at 365 MHz (Texas Survey; Douglas et al. 1996), 1.4 GHz (*uv* matched CGPS; this work) and 16 GHz (AMI; this work). A best-fitting spectral index of $\alpha = 1.3 \pm 1.1$ is shown as a dashed line.

by Clemens & Barvainis (1988) of 10.1 × 2.2 arcmin^2. It is unsurprising therefore that in a later paper CYH91 measure a much larger flux density towards this object than that listed for the *IRAS* association of Parker (1988). Given the large angular extent of the region in the co-added *IRAS* images of CYH91 it seems likely that these flux densities will come from an area covering the emission seen in the AMI data.

Previous greybody fits to L1246's SED have suggested T_d = 19 K (Launhardt et al. 1997; Visser et al. 2001) using data at λ > 100 μm. The temperatures found using *IRAS* data alone are higher. From the *IRAS* PSC the temperatures found using 100 to 60, 60 to 25 and 25 to 12 μm are 31, 66 and 101 K, respectively. From the deep *IRAS* photometry of CYH91 using a much larger aperture the same temperatures are 31, 69 and 222 K. These fits are sensitive to the angular size assumed for the object, the discrepancy at 12 μm suggests a significant change in morphology at that wavelength.

The morphology of the AMI data at 16 GHz appears to trace the 12-μm emission and to a lesser extent the 100-μm emission also. Taking a 5 arcmin^2 region around the emission seen in the AMI data to the east of the pointing centre there is a slightly higher spatial correlation between the emission seen at 12 μm ($r = 0.70$) with that seen at 16 GHz than there is at 100 μm ($r = 0.61$). There is no source coincident with the AMI emission at either 1.4 or 2.7 GHz. The AMI data itself towards this source is poor due to interference and the combined channel map is heavily weighted towards channel 6 (16.4 GHz) making a determination of the spectrum using AMI data alone unreliable.

5 DISCUSSION AND CONCLUSIONS

Of the 14 clouds observed here two are clear candidates for possessing anomalous dust emission at 16 GHz: L675 and L1111. A further three are possible candidates: L944, L1103 and L1246. Nine of the 14 showed no emission inconsistent with that seen at lower radio frequencies.

We divide the five clouds where there is an excess of emission into two groups on the basis of three criteria: (1) extent of the emission seen at 16 GHz, i.e. non-point-like sources; (2) coincident with the sub-mm position of the cloud to within a 2-arcmin radius; (3) likelihood of alternative explanations for the 16-GHz emission.

We summarize our results in Table 3. Column (5) of Table 3 summarizes which dark clouds have a possible spinning dust

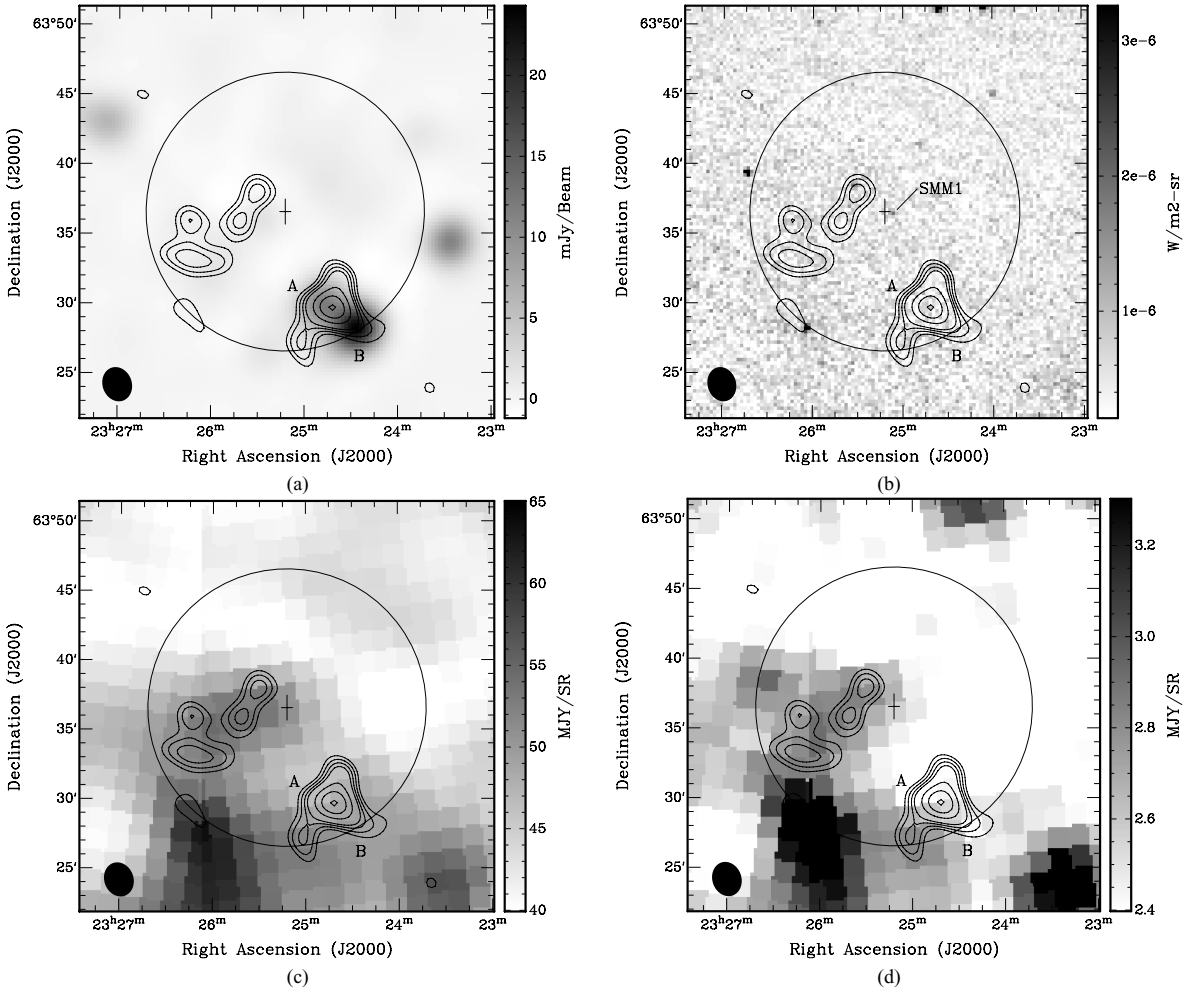

Figure 21. L1246: AMI 16 GHz combined channel data are shown as contours at 3, 4, 5, 6, 9, 12 and 15σ. Grey-scale is (a) *uv* matched CGPS data at 1.4 GHz, (b) 8-μm MSX (band A) data, (c) 100-μm *IRAS* data and (d) 12-μm *IRAS* data. In plot (a) the position of the protostar SMM1 is indicated and in plots (c) and (d) the position of the associated *IRAS* point source is shown as a square. In all plots the AMI pointing centre is shown as a cross and the primary beam as a solid circle. The AMI synthesized beam, 2.5 × 2.2 arcmin^2, is shown as a filled ellipse at the bottom left of each image. The intensity in the MSX and IRIS images is saturated at both ends of the scale in order to make the structure in this region visible.

Table 3. 16 GHz dust emissivities relative to 100 μm emission. Column (1) source name, column (2) predicted intensity based on an emissivity of 10 μK (MJy/sr)$^{-1}$, column (3) measured intensity towards phase centre, column (4) measured 16 GHz dust emissivity relative to IRIS 100-μm data, column (5) possible identification of a spinning dust counterpart as described in Section 5, columns (6–8) certainty criteria as described in Section 5. Bold font indicates positive detection.

Name	$S_{\rm pred}$ (mJy beam^{-1})	$S_{\rm act}$ (mJy beam^{-1})	ϵ μK (MJy/sr)$^{-1}$	Possible identification	Criterion [1]	[2]	[3]
L675	3.6	5.9 ± 0.3	16.4 ± 1.8	y	y	y	n
L709	2.8	−0.8 ±0.3	<0	n	–	–	–
L860	4.2	3.0 ± 0.3	7.2 ± 1.0	n	–	–	–
L917	7.9	−0.7 ±0.3	<0	n	–	–	–
L944	2.7	1.7 ± 0.3	6.2 ± 1.3	y	n	y	n
L951	1.9	−0.9 ±0.3	<0	n	–	–	–
L953	2.4	1.1 ± 0.6	4.5 ± 2.5	n	–	–	–
L1014	2.5	0.0 ± 0.4	0.0	n	–	–	–
L1021	2.8	1.0 ± 0.4	3.5 ± 1.4	n	–	–	–
L1103	4.7	1.8 ± 0.5	3.9 ± 1.2	y	y	y	y
L1111	3.1	8.7 ± 0.5	28.5 ± 3.3	y	y	y	n
L1166	1.5	0.3 ± 0.6	2.0 ± 4.0	n	–	–	–
L1185	4.2	−0.4 ±1.1	<0	n	–	–	–
L1246	2.1	0.2 ± 0.4	1.0 ± 2.0	y	n	y	n

association, defined as being a microwave counterpart within a 2-arcmin radius which shows an excess at 16 GHz relative to lower frequency data. Columns (6–8) then divide the certainty of these detections based on the three criteria stated in the previous paragraph.

On the basis of these three criteria we see that all are satisfied by L675 and L1111 which display extended emission coincident with the pointing centre. The extended nature of this emission makes the possibility of the emission being cm-wave radiation from either a protostar or protoplanetary disc unlikely. L944 shows compact emission which is coincident with the pointing centre. The compact nature of this emission means that cm-wave radiation from a protostar cannot be ruled out in this case. L1246 shows emission just within a radius of 2 arcmin from the SCUBA position of this cloud which has no lower frequency counterpart. However, the compact nature of this emission suggests that it may again be cm-wave emission from a protostar.

L1103 shows extended emission which is coincident with the pointing centre. However, although the microwave spectrum appears to be consistent with emission from spinning dust this source has a high flux density at 850 μm (Visser et al. 2001) relative to *IRAS* measurements at 12–100 μm (CYH91). This raises questions over the suitability of a standard greybody fit to the thermal dust emission from this cloud and, in the absence of further observations between 100 and 300 GHz, it is not possible to rule out a flattened tail to the thermal dust spectrum which may account for the excess seen at 16 GHz.

In their theoretical models for the emission from rotating grains DL98 considered a number of gas-grain, plasma and radiative contributions to the excitation and damping of spinning dust grains. For their several models of grain environment it was found that collisions with ions were the dominant excitation mechanism in all but two scenarios: reflection nebulae and photodissociation regions, where photoelectric effects dominated due to the intense radiation field. For the environments relevant to dark nebulae (MC and cold neutral medium environments) this suggests that objects which are embedded in or exposed to strongly ionized environments are the most likely candidates for observing spinning dust emission. The presence of an anomalous component in the spectra of the objects presented here appears to be correlated with the average free–free emission within a 1° area centred on each pointing centre, see Fig. 22. We assess this correlation following the method of Franzen et al. (2009), where we express the covariance matrix of our data points, C, as

$$C = S + N_i \tag{5}$$

$$= \begin{pmatrix} S_{11} & S_{12} \\ S_{21} & S_{22} \end{pmatrix} + \begin{pmatrix} \sigma_{x,i}^2 & 0 \\ 0 & \sigma_{y,i}^2 \end{pmatrix}. \tag{6}$$

S_{11} and S_{22} are the variances of the 2.7 and 16 GHz data points, respectively, and $S_{12}(= S_{21})$ is the covariance of the 2.7 and 16 GHz data points. It follows that the correlation coefficient, denoted R to distinguish it from the standard Pearson coefficient, is given by

$$R = \frac{S_{12}}{\sqrt{S_{11} S_{22}}}. \tag{7}$$

Following Franzen et al. (2009) we used a Gaussian likelihood and the nested sampling algorithm implemented in the MULTINEST code (Feroz & Hobson 2008; Feroz, Hobson & Bridges 2008) to obtain R. For the averaged 2.7-GHz flux density we find a correlation coefficient of $R = 0.81 \pm 0.15$. For the 2.7-GHz flux density at the position of the cloud with the 16-GHz flux density at the same position we find a weaker correlation, $R = 0.66 \pm 0.20$. We repeated these evaluations setting the noise covariance matrix to zero and found values of $R = 0.70 \pm 0.18$ and 0.65 ± 0.20 for the averaged flux density at 2.7 GHz and the 2.7-GHz flux density at the position of the cloud, respectively. We can see that the noise in the first instance leads to a decrease in correlation unless it is accounted for.

Of the 14 clouds observed, those with the highest background levels at 2.7 GHz are L675, L1111, L860 and L1103; all of which have a background level above 100 mK. Indeed the correlation is

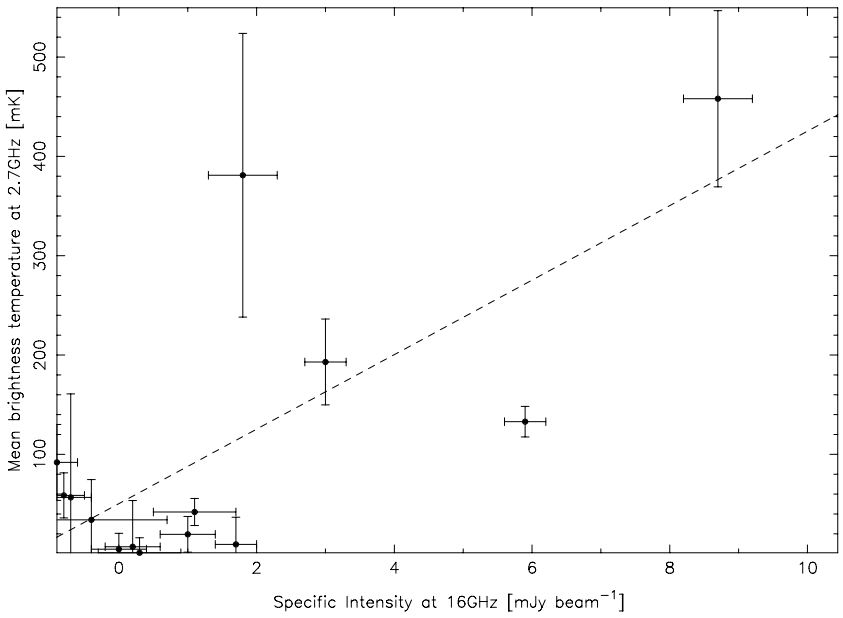

Figure 22. Correlation of mean radio brightness temperature with microwave specific intensity towards observation pointing centres. Data are specific intensity at 16 GHz towards the SCUBA position of the dark cloud on the x-axis, and mean brightness temperature within a 1° diameter circle centred on the position of the dark cloud on the y-axis. The error bars on this mean show the standard deviation of the brightness temperature distribution within this region.

dominated by the high surface brightness regions, suggesting a radio surface brightness threshold between those regions which exhibit spinning dust emission and those which do not.

There appears to be no correlation between 16-GHz specific intensity and 100-μm emission. Following the same correlation analysis described in equation (7) we obtain a value of $R = 0.02 \pm 0.32$ ($R = -0.01 \pm 0.32$ without noise). The dust emissivity at 16 GHz relative to the *IRIS* 100-μm data is tabulated in Table 3. We also list the predicted specific intensities for these objects for a relative emissivity of 10 μK (MJy /sr)$^{-1}$ for reference. The relative emissivity of our two strongest detections is similar to that found for LDN 1622 (Casassus et al. 2006) and G159.618.5 (Watson et al. 2005). This suggests that the non-detections in our sample are not an effect of our sensitivity limits. If the emissivity of anomalous microwave emission relative to that seen at 100 μm was at a similar level in all dark clouds, for example >10 μK (MJy/sr)$^{-1}$, then we would have detected emission from every cloud in our sample at $>3\sigma_{\rm rms}$. The weighted average dust emissivity relative to the 100-μm maps for our sample is 6.6 ± 5.0 μK (MJy/sr)$^{-1}$. This value agrees with the all-sky *WMAP* (*Wilkinson Microwave Anisotropy Probe*) value for cool dust clouds at high galactic latitudes (Davies et al. 2006), given as 1 Jy at 30 GHz per 6000 Jy at 100 μm.

Of our five possibly anomalous objects two are known to be class 0 objects: L944 and L1246. High sensitivity maps in CO towards our two most anomalous objects do not yet exist and they are assumed starless. However, the starless/protostellar divide has come under scrutiny recently following the discovery of Very Low Luminosity Objects (VeLLOs) with *Spitzer*. VeLLOs are faint infrared point sources with protostellar colours towards objects previously classified as starless. Young et al. (2004) discovered a VeLLO in L1014 (L1014-IRS), part of the Visser et al. sample, coincident with the peak of dust continuum emission that had been previously classified as starless by Parker (1988). Although here no anomalous microwave emission is seen towards L1014 it is suggestive that the peak of the anomalous emission towards L944 is more coincident with the centre of the red-shifted CO $2 \rightarrow 1$ outflow lobe, mapped by Visser et al., and not the compact SCUBA emission from the class 0 protostar. This spatial correspondence immediately raises the question of whether the outflow itself or possibly the cloud turbulence could be energizing the spinning dust emission. Regardless of this possible connection we also point out that the misidentification of radio emission from protostars is a potential source of confusion when searching for emission from spinning dust.

There seems to be no obvious correlation between the AMI flux densities and the *IRAS* or SCUBA flux densities, however, the number of data points is low. It is also true that there is no correlation between the SCUBA flux densities at 850 μm and those of *IRAS* at 100 μm. This is perhaps not particularly surprising in light of the mismatch in measured angular scales, and would suggest that the morphology of these objects is larger at 850 μm than the SCUBA chop allows for. Obviously this is not a problem when investigating compact cores as in Visser et al. (2001, 2002), however, it provides little assistance when looking at the correlation between cm-wave and mm-wave emission.

In conclusion, we have observed a sample of 14 compact Lynds dark nebulae. We have found a significant excess towards two of the 14 and an indication of anomalous behaviour in three further clouds. We suggest that the excess we see is due to rotational emission from very small grains and that this emission may be correlated with a high level of background emission at lower radio frequencies.

ACKNOWLEDGMENTS

We thank the staff of the Lord's Bridge Observatory for their invaluable assistance in the commissioning and operation of the Arcminute Microkelvin Imager. We thank John Richer for useful discussions. We also thank the anonymous referee, whose comments have significantly improved this paper. The AMI is supported by Cambridge University and the STFC. NH-W, MLD, TMOF, CR-G and TWS acknowledge the support of PPARC/STFC studentships.

REFERENCES

Andre P., Ward-Thompson D., Barsony M., 1993, ApJ, 406, 122
Baars J. W. M., Genzel R., Pauliny-Toth I. I. K., Witzel A., 1977, A&A, 61, 99
Bourke T. L., Crapsi A., Myers P. C., Evans N. J., II, Wilner D. J., Huard T. L., Jørgensen J. K., Young C. H., 2005, ApJ, 633, L129
Calabretta M., 1991, Australian J. Phys., 44, 441
Casassus S., Cabrera G. F., Förster F., Pearson T. J., Readhead A. C. S., Dickinson C., 2006, ApJ, 639, 951
Casassus S., Nyman L.-A., Dickinson C., Pearson T. J., 2007, MNRAS, 382, 1607
Casassus S. et al., 2008, MNRAS, 391, 1075
Clemens D. P., Barvainis R., 1988, ApJS, 68, 257
Clemens D. P., Yuo J. L., Heyer M. H., 1991, ApJS, 75, 877 (CYH91)
Condon J. J., Cotton W. D., Greisen E. W., Yin Q. F., Perley R. A., Taylor G. B., Broderick J. J., 1998, AJ, 115, 1693
Davies R. D., Dickinson C., Banday A. J., Jaffe T. R., Górski K. M., Davis R. J., 2006, MNRAS, 370, 1125
Dickinson C., Davies R. D., Bronfman L., Casassus S., Davis R. J., Pearson T. J., Readhead A. C. S., Wilkinson P. N., 2007, MNRAS, 379, 297
Douglas J. N., Bash F. N., Bozyan F. A., Torrence G. W., Wolfe C., 1996, AJ, 111, 1945
Draine B. T., 2003, ARA&A, 41, 241
Draine B. T., Lazarian A., 1998, ApJ, 508, 157 (DL98)
Erickson W. C., 1957, ApJ, 126, 480
Feroz F., Hobson M. P., 2008, MNRAS, 384, 449
Feroz F., Hobson M. P., Bridges M., 2008, preprint (arXiv:0809.3437)
Ferrara A., Dettmar R.-J., 1994, ApJ, 427, 155
Franco J., Kurtz S., Hofner P., Testi L., García-Segura G., Martos M., 2000, ApJ, 542, L143
Franzen T. M. O. et al., 2009, preprint (arXiv:0907.3843)
Froebrich D., 2005, ApJS, 156, 169
Fürst E., Reich W., Reich P., Reif K., 1990, A&AS, 85, 805
Green D. A., 2007, Bull. Astron. Soc. India, 35, 77
Gregory P. C., Scott W. K., Douglas K., Condon J. J., 1996, ApJS, 103, 427
AMI Consortium: Hurley-Walker N. et al., 2009, MNRAS, in press (arXiv:0902.1420)
Kogut A., Banday A. J., Bennett C. L., Górski K. M., Hinshaw G., Reach W. T., 1996, ApJ, 460, 1
Launhardt R., Ward-Thompson D., Henning T., 1997, MNRAS, 288, L45
Leitch E. M., Readhead A. C. S., Pearson T. J., Myers S. T., 1997, ApJ, 486, L23
Lynds B. T., 1962, ApJS, 7, 1
Miville-Deschênes M.-A., Lagache G., 2005, ApJS, 157, 302
Parker N. D., 1988, MNRAS, 235, 139
Parker N. D., 1991, MNRAS, 251, 63
Patnaik A. R., Browne I. W. A., Wilkinson P. N., Wrobel J. M., 1992, MNRAS, 254, 655
Reich P., Reich W., Fürst E., 1997, A&AS, 126, 413
Rengelink R. B., Tang Y., de Bruyn A. G., Miley G. K., Bremer M. N., Roettgering H. J. A., Bremer M. A. R., 1997, A&AS, 124, 259
Scaife A. et al., 2007, MNRAS, 377, L69
AMI Consortium: Scaife A. M. M. et al., 2008, MNRAS, 385, 809
AMI Consortium: Scaife A. M. M. et al., 2009, MNRAS, 394, L46
Schlegel D. J., Finkbeiner D. P., Davis M., 1998, ApJ, 500, 525

Shirley Y. L., Claussen M. J., Bourke T. L., Young C. H., Blake G. A., 2007, ApJ, 667, 329
Stamatellos D., Ward-Thompson D., Whitworth A. P., Bontemps S., 2007, A&A, 462, 677
Taylor A. R. et al., 2003, AJ, 125, 3145
Visser A. E., Richer J. S., Chandler C. J., 2001, MNRAS, 323, 257
Visser A. E., Richer J. S., Chandler C. J., 2002, AJ, 124, 2756
Watson R. A., Rebolo R., Rubiño-Martín J. A., Hildebrandt S., Gutiérrez C. M., Fernández-Cerezo S., Hoyland R. J., Battistelli E. S., 2005, ApJ, 624, L89
Young C. H. et al., 2004, ApJS, 154, 396
AMI Consortium: Zwart J. T. L. et al., 2008, MNRAS, 391, 1545

APPENDIX A: AMI MAPS

This appendix contains maps of the CLEANed AMI combined channel data towards each of the SCUBA dark cloud positions (see Fig. A1). Images are shown in grey-scale and contours. The grey-scale is not saturated and contours are shown at ±3, ±6, $\pm12\sigma$ etc, where σ is listed for each observation in Table 1. The AMI primary beam is shown as a circle and the synthesized beam as a filled ellipse in the bottom left-hand corner.

APPENDIX B: FLUX EXTRACTION POLYGONS

This appendix contains tables of the polygon vertices used for flux extraction in regions of more complex emission. These tables are ordered by object as denoted in Figs 2–16 and contain vertices for five polygons per object. The columns of these tables are: (1) right ascension (J2000), (2) declination (J2000) and (3) a true/false flag denoting whether this vertex was used (T), or not (F), for fitting a tilted plane within the polygon. These polygons were used as

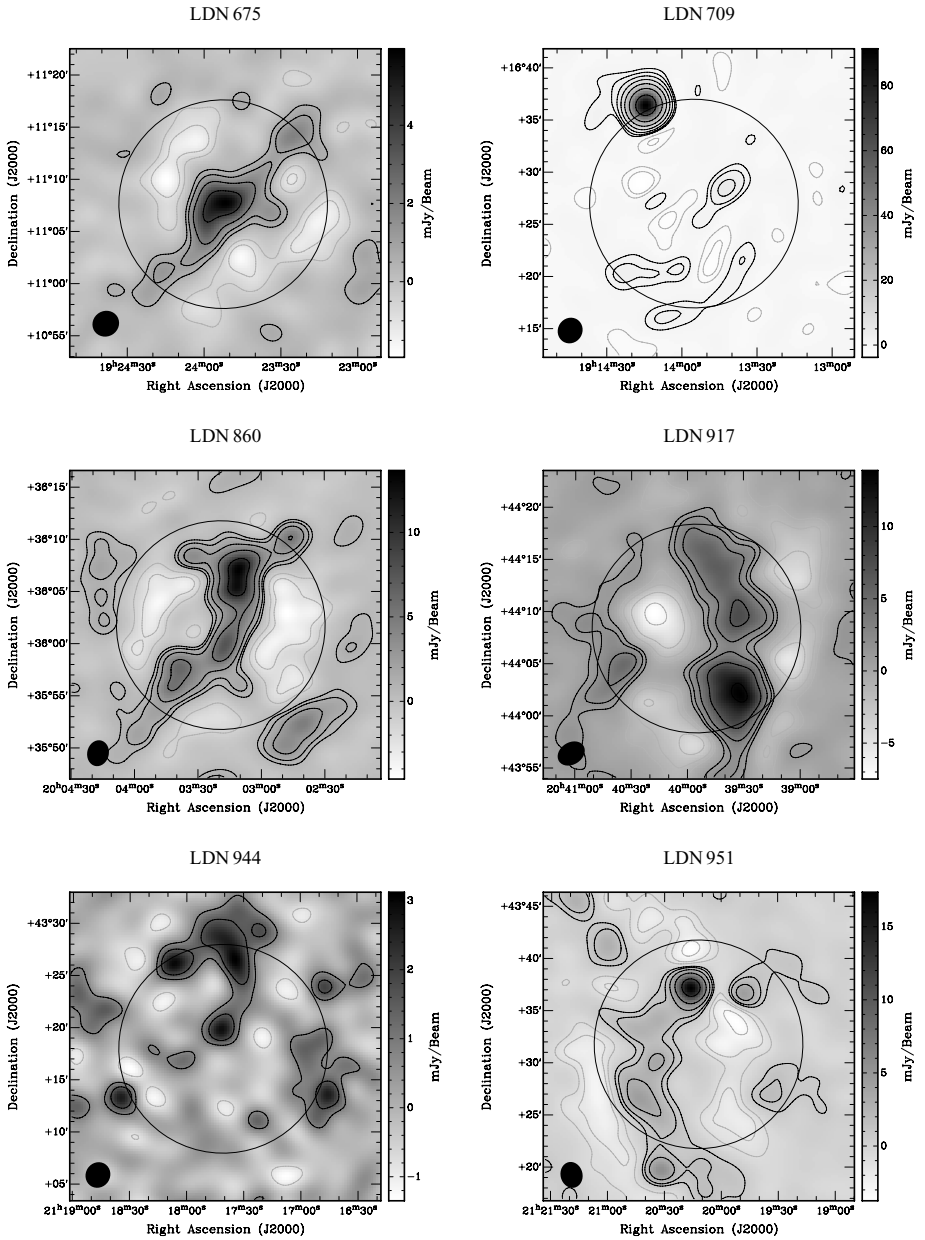

Figure A1. CLEANed AMI combined channel maps of Lynds dark nebulae. Maps are not primary beam corrected. The FWHM of the AMI beam is indicated as a black circle and the synthesized beam as a filled ellipse in the bottom left-hand corner of each map. Contours are shown at ±3, ±6, ±12 σ etc.

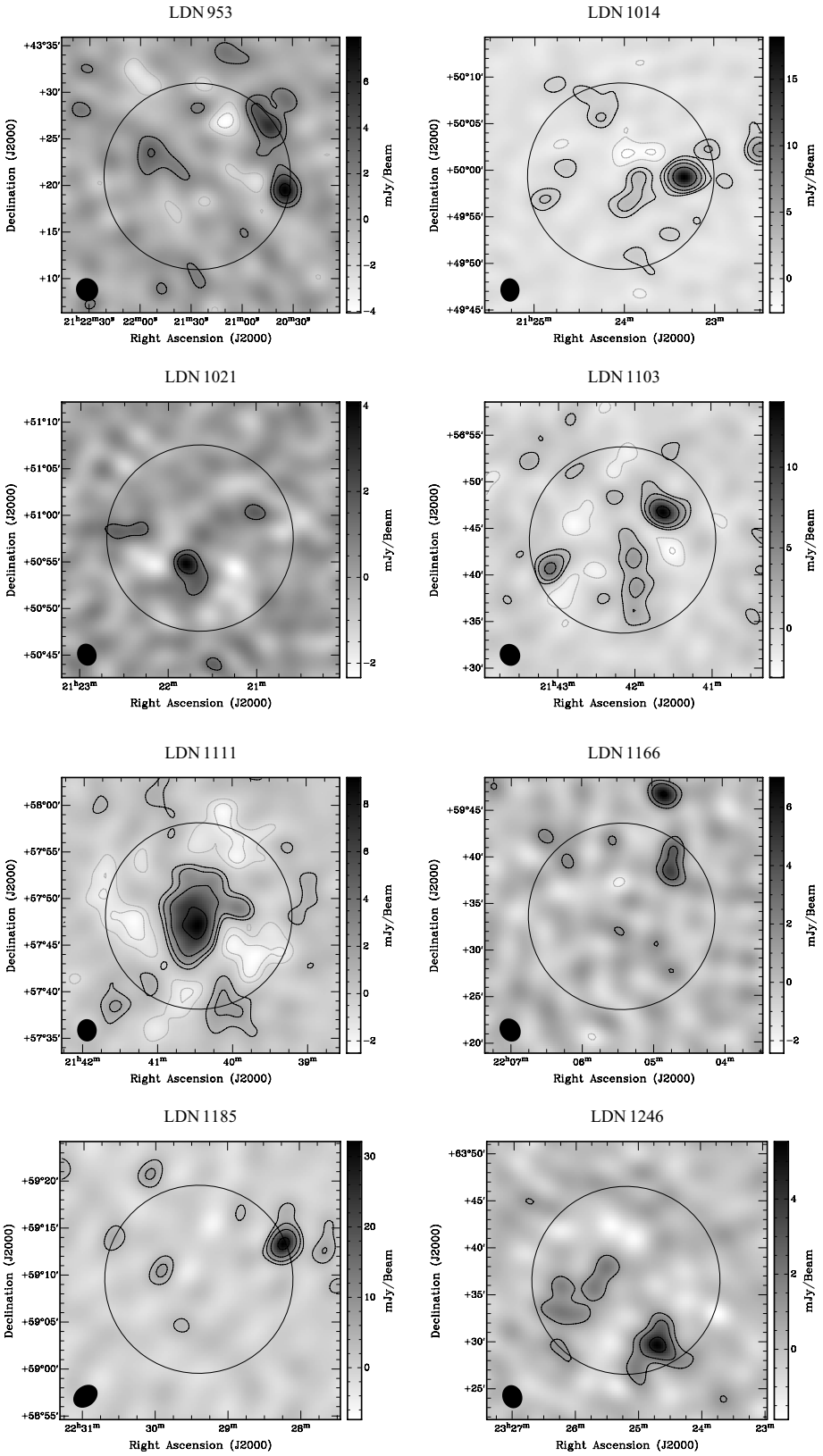

Figure A1 – *continued*

Table B1. Flux extraction polygons for L675.

L675								
Polygon 1: 20.5 mJy			Polygon 3: 20.0 mJy			Polygon 5: 19.5 mJy		
19:23:48.084	+11:14:40.30	F	19:23:45.331	+11:15:30.25	F	19:23:39.399	+11:13:05.33	F
19:23:18.171	+11:08:51.58	F	19:23:22.470	+11:10:02.56	F	19:23:24.591	+11:09:37.37	F
19:23:19.017	+11:09:04.18	T	19:23:22.043	+11:09:43.65	T	19:23:24.591	+11:09:37.37	T
19:23:23.255	+11:03:53.41	T	19:23:26.710	+11:03:50.88	T	19:23:23.742	+11:05:06.46	T
19:24:04.448	+10:58:46.88	T	19:24:01.841	+11:00:29.34	T	19:23:46.183	+11:01:19.75	T
19:24:13.473	+10:59:03.65	T	19:24:17.070	+10:59:51.49	T	19:24:15.378	+10:58:35.90	T
19:24:32.939	+11:03:07.13	T	19:24:23.418	+11:00:29.25	T	19:24:33.560	+10:58:23.18	T
19:24:23.357	+11:06:28.80	T	19:24:23.843	+11:04:22.35	T	19:24:27.233	+11:02:54.13	T
19:24:14.895	+11:11:39.65	T	19:24:14.120	+11:10:59.30	T	19:24:16.654	+11:07:56.59	T
19:23:56.832	+11:14:57.10	T	19:24:01.420	+11:15:05.04	T	19:24:07.770	+11:11:49.73	T
Polygon 2: 20.8 mJy			Polygon 4: 19.7 mJy			19:23:47.442	+11:14:02.05	T
						19:28:13.541	+11:13:55.02	T
19:23:46.596	+11:14:58.75	F	19:23:44.904	+11:13:55.74	F			
19:23:20.352	+11:08:59.54	F	19:23:24.591	+11:09:43.67	F			
19:23:18.244	+11:08:15.43	T	19:23:24.591	+11:09:43.67	T			
19:23:21.207	+11:04:03.45	T	19:23:25.864	+11:03:31.98	T			
19:23:38.562	+11:01:38.63	T	19:23:52.947	+11:01:32.35	T			
19:24:03.103	+10:59:07.44	T	19:24:11.568	+10:58:54.81	T			
19:24:22.572	+10:59:57.76	T	19:24:24.679	+10:59:07.34	T			
19:24:28.499	+11:04:28.62	T	19:24:26.377	+11:02:54.13	T			
19:24:22.585	+11:07:37.66	T	19:24:18.343	+11:06:03.18	T			
19:24:14.538	+11:11:30.80	T	19:24:09.043	+11:10:59.32	T			
19:24:00.146	+11:15:11.34	T	19:23:50.409	+11:14:02.05	T			

described in Section 3.2. An example table for L675 is shown in Table B1, and details of the remaining flux extraction polygons may be found in the online version of this paper (Tables B1–B20; see Supporting Information).

SUPPORTING INFORMATION

Additional Supporting Information may be found in the online version of this article:

Appendix B. Flux extraction polygons.

Please note: Wiley-Blackwell are not responsible for the content or functionality of any supporting materials supplied by the authors. Any queries (other than missing material) should be directed to the corresponding author for the article.

This paper has been typeset from a TEX/LATEX file prepared by the author.